Available online at www.sciencedirect.com

ScienceDirect

Geochimica et Cosmochimica Acta 318 (2022) 366–387

Geochimica et Cosmochimica Acta

www.elsevier.com/locate/gca

Using whole rock and in situ pyrite chemistry to evaluate authigenic and hydrothermal controls on trace element variability in a Zn mineralized Proterozoic subbasin

Joseph M. Magnall [a,*], Sarah A. Gleeson [a,b], Nicholas Hayward [c], Marcus Oelze [a]

[a] GFZ German Research Centre for Geosciences, 14473 Potsdam, Germany
[b] Institute of Geological Sciences, Freie Universität Berlin, Malteserstrasse, 74-100, Berlin 12249, Germany
[c] Teck Australia Pty Ltd, PO Box 1677, WA 6872, Australia

Received 30 April 2021; accepted in revised form 1 December 2021; available online 10 December 2021

Abstract

The mid-Proterozoic stratigraphy of the McArthur Basin (Australia) contains some of the most well-preserved sedimentary rocks of Precambrian age, which are also host to giant, clastic dominant (CD-type) massive sulfide Zn deposits. The most recently discovered CD-type deposit (the Teena deposit) is located in the Teena subbasin and hosted by the 1.64 Ga Barney Creek Formation. The Teena subbasin, therefore, provides the perfect natural laboratory for evaluating authigenic and hydrothermal controls on trace element (TE) variability, both of which contribute to paleoenvironmental reconstructions and ore deposit models. As the Teena deposit formed beneath the paleoseafloor, this also provides the opportunity to evaluate TE zonation around a fossilized subseafloor replacement hydrothermal system. In situ laser ablation inductively coupled mass spectrometry (LA-ICP-MS) has been used to define compositional end members in diagenetic and hydrothermal pyrite. The overgrowth of hydrothermal sulfides on diagenetic pyrite is associated with TE anomalism (Tl, Pb, As, Zn) that extends > 100 meters above the main high grade sulfide mineralization the Teena subbasin. The vertical zonation in TEs is consistent with the infiltration of hydrothermal fluids into overlying hangingwall sediments that were undergoing diagenesis. Bulk rock lithogeochemical data record covariation between total organic carbon (TOC) and a suite of TEs (Mo, Co, Ni, V). We suggest this was caused by local hydrographic factors during deposition of the Barney Creek Formation. High TOC/P molar ratios, resulting from regeneration of P in a euxinic water column, are associated with an interval overlying the main maximum flooding surface in the subbasin. The relationships between TOC, P and TEs resemble the redox architecture of a silled basin rather than an open marine margin. Sulfidic conditions developed during periods of high productivity, which were linked to nutrient supply that was enhanced by connectivity with surrounding water masses. The evidence of redox bistability, involving a delicate balance between ferruginous (anoxic, non-sulfidic) and euxinic (sulfidic) conditions, is consistent with recent models for other mid-Proterozoic sedimentary units. Nevertheless, there was a strong localised (10^1 km^2) control on the authigenic and hydrothermal TE chemistry of the Barney Creek Formation in the Teena subbasin, which highlights a key challenge when extrapolating from data collected in partially restricted intracontinental marine settings.

Keywords: Proterozoic; McArthur Basin; Zn resources; TEs; Intracontinental basin; Pyrite chemistry; LA-ICP-MS; Barney Creek Formation

1. INTRODUCTION

The composition of marine sedimentary rocks and their constituent mineral phases are controlled by processes

* Corresponding author.
E-mail address: magnall@gfz-potsdam.de (J.M. Magnall).

https://doi.org/10.1016/j.gca.2021.12.001
0016-7037/

(detrital, biogenic, authigenic, hydrothermal) that operate on a variety of scales (Sageman and Lyons, 2003). Reconstructions of these processes from whole rock lithogeochemistry or in situ mineral chemistry datasets provide the foundations for models of both ancient paleoenvironments and hydrothermal ore deposits (e.g. Large et al., 2014; Gregory et al., 2019; Wei and Algeo, 2020). One nexus between these two research areas can be found in the mid-Proterozoic McArthur Basin, which contains some of the most well-preserved Precambrian sedimentary rocks and a number of world class clastic dominant (CD-type) Zn deposits (Brocks et al., 2005; Large et al., 2005).

A common feature of mudstones and modern organic-rich sediments is their combined enrichment in both pyrite and TEs (TEs; e.g. Mo, Ni, Co, V), and for decades, these components have been analysed using whole rock techniques (Berner, 1984; Tribovillard et al., 2006). Whole rock techniques are time consuming and most suited to homogenous samples, but they also enable the quantification of most elements from the periodic table in a diverse range of samples. The partitioning of many TEs into pyrite has meant that over recent years, pyrite has become a target for *in situ* laser ablation inductively coupled plasma mass spectrometry (LA-ICP-MS), with benefits including rapid data generation and greater sensitivity relative to bulk rock methods (Danyushevsky et al., 2011; Large et al., 2014). The LA-ICP-MS analysis of pyrite is not without some challenges however, and includes: (1) the time-consuming nature of generating petrographic data and development of subjective paragenetic arguments; (2) mixed analyses when analysing inclusion rich or fine-grained samples (Stepanov et al., 2020), and; (3) heterogeneous reference materials that compromise the accurate quantification of data (Wohlgemuth-Ueberwasser et al., 2007). Nevertheless, combining whole rock and LA-ICP-MS analyses can help to mitigate and augment the respective datasets (e.g. Gregory et al., 2017).

Pyrite can form in a range of low, and high, temperature environments and provides a valuable archive of TE and isotopic data in geological samples (Rickard and Luther, 2007). In a range of hydrothermal ore deposit types pyrite is commonly part of the pre-, syn-, and post-mineralization assemblages, and *in situ* analyses of pyrite have been used to delineate spatial and temporal variability of TEs in paragenetically complex samples (e.g. Reich et al., 2013; Ingham et al., 2014; Genna and Gaboury, 2015; Gadd et al., 2016). A number of studies have also focused on sulfide TE chemistry in modern seafloor massive sulfide (SMS) deposits and the ancient volcanogenic massive sulfide (VMS) deposits that are analogues to these systems (e.g. Maslennikov et al., 2009; Keith et al., 2016; Grant et al., 2018). Yet far less is known about sulfide chemistry and TE dispersion around CD-type deposits, which are much larger than VMS deposits and have no known modern analogues.

The paragenesis and environment of sulfide mineralization (seafloor vs. subsurface) in CD-type deposits has major implications for how TE chemistry is interpreted in sedimentary basins. In the broadest sense, basin scale constraints on paleoenvironmental conditions (e.g. euxinic periods) are often extrapolated from models where CD-type deposits are considered to have formed via sedimentary exhalative (SEDEX) processes (e.g. Johnston et al., 2008). From an exploration perspective, TE anomalism in diagenetic pyrite might be considered to result from long range (10^3-10^4 m) lateral halos of hydrothermally sourced metals in seawater, which are sequestered by pyrite formed either in the water column or the earliest stages of diagenesis (e.g. Mukherjee and Large, 2017). In contrast, TE dispersion associated with host rock replacement beneath the seafloor will be controlled by reaction permeability and may be concentrated in discrete, low volume, generations of pyrite that have a limited lateral extent. Uncertainty over which of these models is most applicable limits both the practical potential of pyrite chemistry datasets in vectoring towards undiscovered deposits and the accuracy of regional paleoenvironmental reconstructions.

In this study, we focus on new drill-cores from the McArthur Basin (Fig. 1) that intersect the Barney Creek Formation (BCF) in the Teena subbasin (Fig. 2). The BCF contains some of the most well-preserved biomarkers of Precambrian age that record evidence of photic zone euxinia (e.g. Brocks et al., 2005). The expansion of euxinic conditions during the mid-Proterozoic has been linked to some fundamental changes in the earth system, including the disappearance of Precambrian Fe formations around 1.85 Ga, together with the drawdown of bioavailable redox sensitive TEs that may have prevented eukaryotic evolution (Li et al., 2015). There has been ongoing revision of the sulfidic ocean model, however, and it is now thought that for much of the Precambrian there were extensive mid-depth euxinic waters in productive regions, with overlying oxygenated surface waters and widespread deep-water ferruginous conditions (Poulton and Canfeld, 2011; Planavsky et al., 2011). This new paradigm for Precambrian ocean redox architecture is typically depicted as a continental margin where water depth progressively deepens away from the shoreline (e.g. Fig. 3A, B). Yet a paucity of passive continental margins during the mid-Proterozoic means it is unclear how applicable this model is for this key time period (Bradley, 2008). In the McArthur Basin, the most reduced, deep-water facies of the BCF are located within fault-bound depocenters in intracratonic subbasins that formed during periods of regional extension (Blaikie and Kunzmann, 2020; Hayward et al., 2021), and more closely resemble a silled basin model (e.g. Fig. 3C). In silled basins, it is much more challenging to decouple compositional trends that relate to changes in the earth system (e.g. atmospheric oxygenation) from those that correspond with more local, subbasin controls (e.g. water mass restriction). In the McArthur Basin, this challenge has been further compounded by varying levels of hydrothermal anomalism, which has provided an additional level of paragenetic and compositional complexity within certain subbasins. As a result, TE variability was likely controlled by a combination of authigenic and hydrothermal processes that operated across different scales, yet few studies have attempted to characterize both. In part, this is due to the challenge of integrating different datasets over the km-thick stratigraphic intervals that are typical of these fault-bound depocenters.

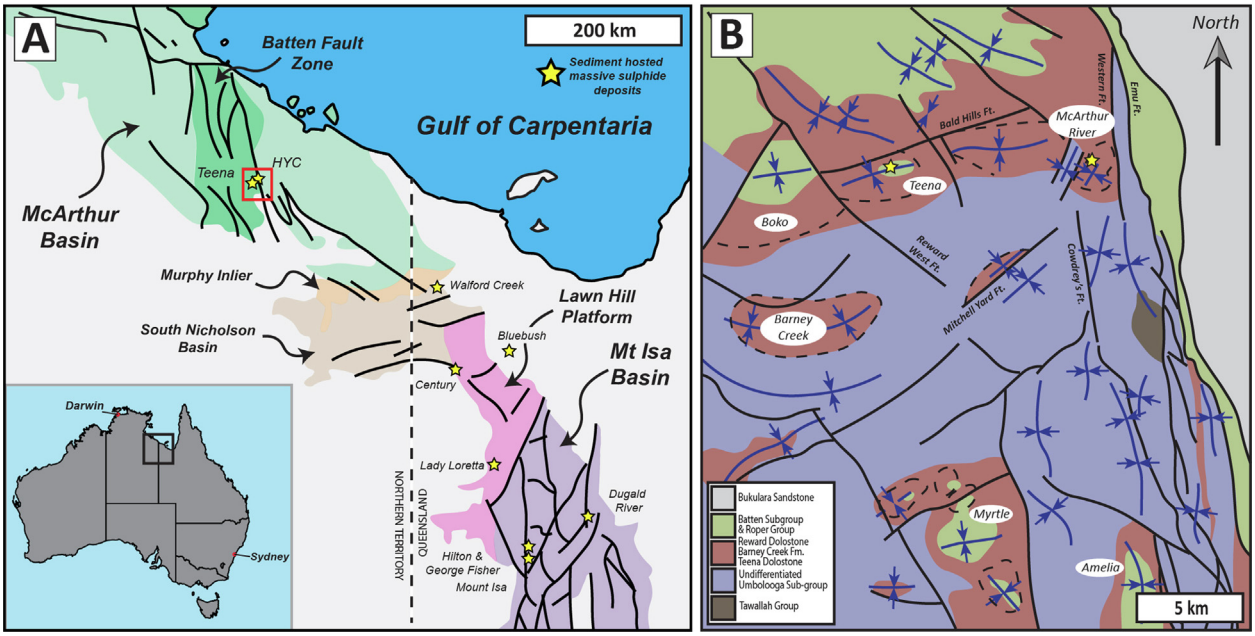

Fig. 1. (A) The Mt Isa Superbasin and locations of major clastic-dominant (CD-type) massive sulfide deposits and prospects (yellow stars). The Teena and McArthur River deposits are located within a southern portion of the Batten Fault Zone (BFZ; red box highlights area shown in B). (B) Simplified geology of the southern BFZ where the Teena and McArthur River deposits are located within synformal, fault-bound depocenters (also referred to as subbasins; demarcated by dashed lines). Modified from Hayward et al., (2021) and McGoldrick et al. (2010).

Recently, the Teena subbasin has been the focus of research that has described the structural, diagenetic and hydrothermal evolution in an integrated model (Hayward et al., 2021; Magnall et al., 2021a). The main stage of hydrothermal sulfide mineralization in the Teena subbasin was emplaced during burial diagenesis of the host rock unit and formed primarily via replacement of dolomite (Hayward et al., 2021; Magnall et al., 2021a). Sulfide mineralization formed at broadly the same time as deposition of the overlying stratigraphic unit, although the nature of TE dispersion around the hydrothermal system has not been evaluated. Studies on TE zonation around CD-type deposits are often inhibited by a lack of stratigraphic continuity around massive sulfide deposits that have undergone subsequent tectonic overprint. The exceptional preservation of the Teena deposit and continuous stratigraphic hanging-wall sequence provides a unique opportunity to evaluate TE anomalism around a subseafloor replacement hydrothermal system.

In this study, we have used bulk rock data to understand background TE variability through a thick stratigraphic interval of the BCF. Pyrite chemistry has then been used to probe samples with a complex paragenesis from within the mineralized unit and explore the dispersion of TEs around a CD-type deposit that formed via host rock replacement during burial diagenesis. We show that there were clear subbasin controls on the availability of TEs within the Teena subbasin that can be attributed to both authigenic and hydrothermal processes. The findings of this study not only improve our understanding of mid-Proterozoic paleoenvironments, but also provide an example for how pyrite chemistry can be used during exploration for massive sulfide deposits in the terrestrial and marine environments.

2. GEOLOGICAL BACKGROUND

2.1. Regional geology

The McArthur Basin is part of the Isa Superbasin, which contains mixed carbonate-siliciclastic sedimentary rocks that were deposited in a large intracratonic setting (0.2×10^6 km^2 outcrop extent; Allen et al., 2015) following the amalgamation of the supercontinent Columbia (known also as Nuna, 880 – 1800 Ma; Giles et al., 2002; Rawlings, 1999). A series of stratigraphic supersequences, deposited between 1.82 to 1.58 Ga, preserve a record of basin extension, depositional hiatus', and basin inversion (Southgate et al., 2000), all of which have been linked to accretionary events on the southern and eastern margin of Columbia (Giles et al., 2002; Betts et al., 2003; Betts et al., 2006). The regional deformation and metamorphic gradient increases toward the south of the Carpentaria Province but in the north, where the Teena deposit is located, the rocks are particularly well-preserved and contain some of the oldest hydrocarbons of Precambrian age (Baruch et al., 2015; Crick et al., 1988). The River Supersequence is host to the majority of clastic sediment-hosted (CD-type) Zn deposits in stratigraphy that is associated with the thermal subsidence phase of rift development (Hayward et al., 2021).

The Teena deposit is hosted by the Barney Creek Formation (BCF) and located within a fault-bound subbasin depocenter (10^1 km^2; Hayward et al. 2021).

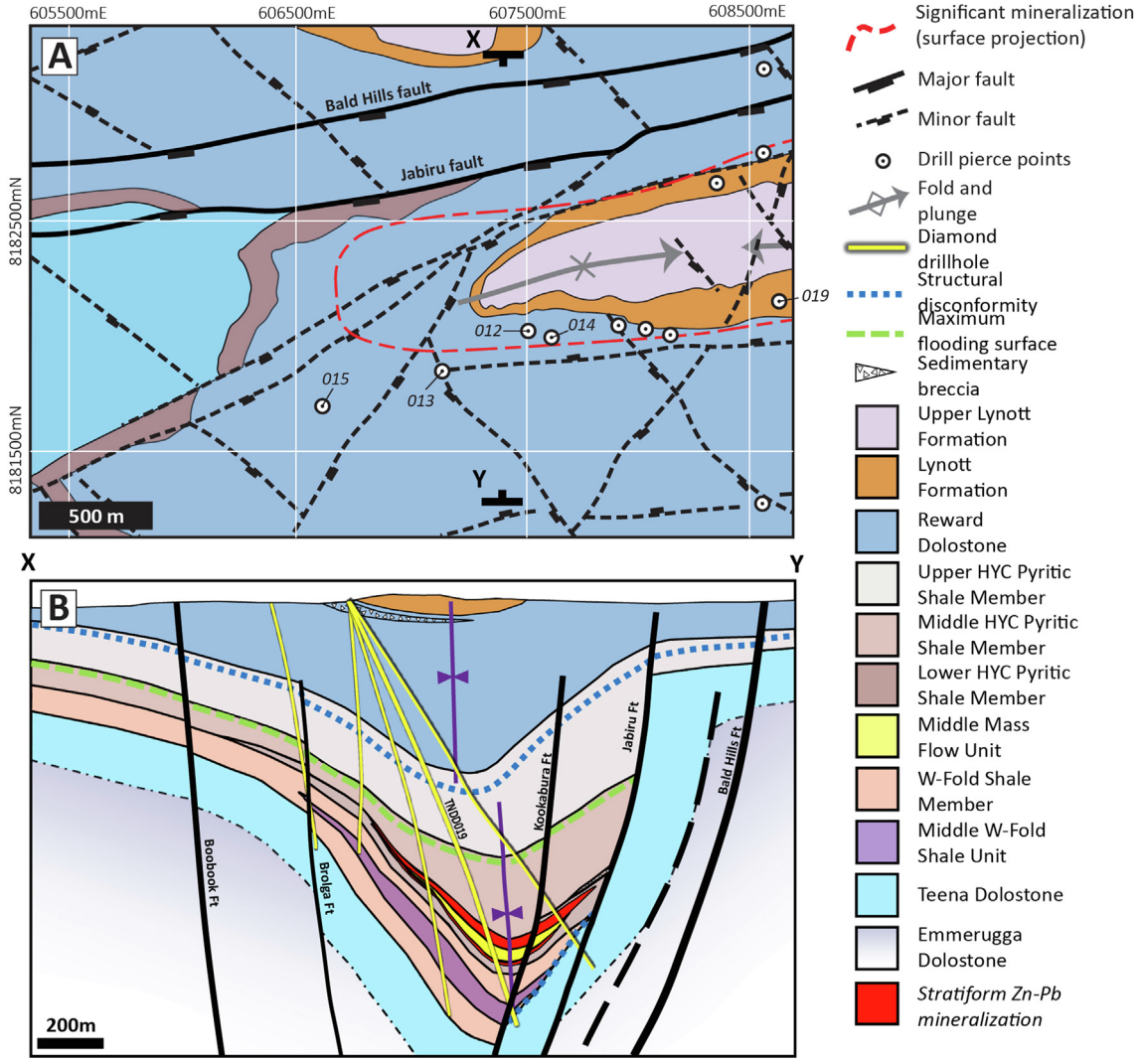

Fig. 2. (A) A geological map of the Teena subbasin annotated with the collars of key drill-holes (white circles) and the projected outline of significant Zn + Pb mineralization are shown (GDA1994 MGA-Z53 coordinates). (B) A geological cross-section through line X-Y at 608600 mE in (A). The main lithological units and the trace of TNDD019 are shown. The Barney Creek Formation is subdivided into the W-Fold Shale Member and Lower, Middle and Upper HYC units. Modified after Magnall et al. (2021a).

The depositional age of the BCF is bracketed by U-Pb zircon ages from interbedded tuffs in the underlying (Teena Dolostone; 1639 ± 6 Ma) and overlying (Lynott Formation; 1636 ± 4 Ma) lithological units (Page et al., 2000). Volcaniclastic sandstone beds in the BCF also contain zircons with ages of 1638 ± 7 Ma, 1639 ± 3 Ma and 1640 ± 3 Ma (Page and Sweet, 1998). The BCF was formally defined following a study on the HYC subbasin (Jackson et al., 1987), and is subdivided into (1) W-Fold Shale Member, (2) HYC Pyritic Shale Member, (3) Cooley Dolostone Member, and (4) undifferentiated upper Barney Creek Formation. Lateral facies changes mean that the Cooley Dolostone Member is not present in the Teena subbasin and instead the BCF has been informally subdivided into four units comprising (Figs. 2, 4): (1) a dolomitic siltstone containing abundant nodular dolostone beds (W-Fold Shale Member), (2) the host rock to the two main sulfide mineralized lenses, which is a carbonaceous, pyritic, dolomitic siltstone that also contains nodular dolomite beds (Lower HYC unit); (3) a variably carbonaceous and dolomitic siltstone that contains a particularly pyritic (>15 wt. % pyrite) interval towards the base (Fig. 4; Middle HYC unit), and; (4) a dolomitic siltstone and sandstone (Upper HYC unit) that transitions into the overlying Reward Dolostone. The Lower and Middle HYC units correspond with the HYC Pyritic Shale Member and the Upper HYC unit with the undifferentiated BCF.

There is considerable variability in thickness and depositional facies in the BCF that can be correlated on a regional scale (Kunzmann et al., 2019). In the Teena subbasin, the W-Fold Shale Member and Lower HYC unit record a deepening cycle of deposition, whereas the Middle and Upper HYC units record a shallowing cycle of deposition. There are also two distinctive 3rd order maximum flooding

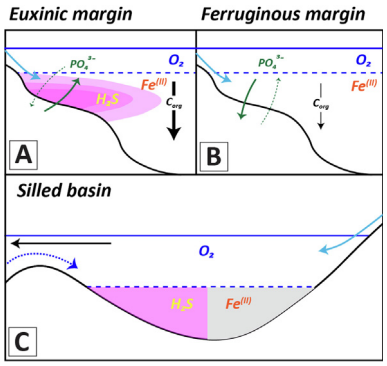

Fig. 3. Schematic diagrams of models for Precambrian redox architecture in a continental margin setting (A + B; modified from Poulton and Canfield (2011) and Guilbaud et al. (2020) and a silled basin (C; modified from Scholz, 2018). In C, the development of ferruginous vs. euxinic conditions is dependent on nutrient supply and sulfate availability.

surfaces (MFS) preserved in the Teena subbasin (Fig. 4; B1 and B2), which have been identified in other subbasins of the Batten Fault Zone (Kunzmann et al., 2019). These MFSs are located at the base of highly pyritic intervals (~50 m) of carbonaceous mudstones that can be correlated from gamma ray logs across the Teena subbasin (Magnall et al., 2021a). Pyrite from the interval overlying the B1 MFS preserves evidence of sulfate limitation in the form of highly positive $\delta^{34}S$ values, which has been linked to the development of euxinic conditions during high levels of localized productivity in the basin (Magnall et al., 2020).

2.2. Mineralization in the Teena subbasin

A number of recent studies have described the sulfide mineralogy and paragenesis in the Teena subbasin (Magnall et al., 2020; 2021a; Hayward et al., 2021). A widespread generation of fine-grained pyrite (py1a) predates nodular dolomite, which are both part of an assemblage that formed during early diagenesis (Hayward et al., 2021). The highest-grade sphalerite mineralized rocks are located in two intervals in the Lower HYC unit (Lower and Main Lenses) and are separated by volcaniclastic sandstone beds (Magnall et al., 2021a, 2021b). There are two main styles of sphalerite mineralization in the Lower and Main Lenses, comprising fine-grained, light brown sphalerite cement (sp1) and coarser-grained red brown sphalerite replacement of nodular dolomite. Both generations

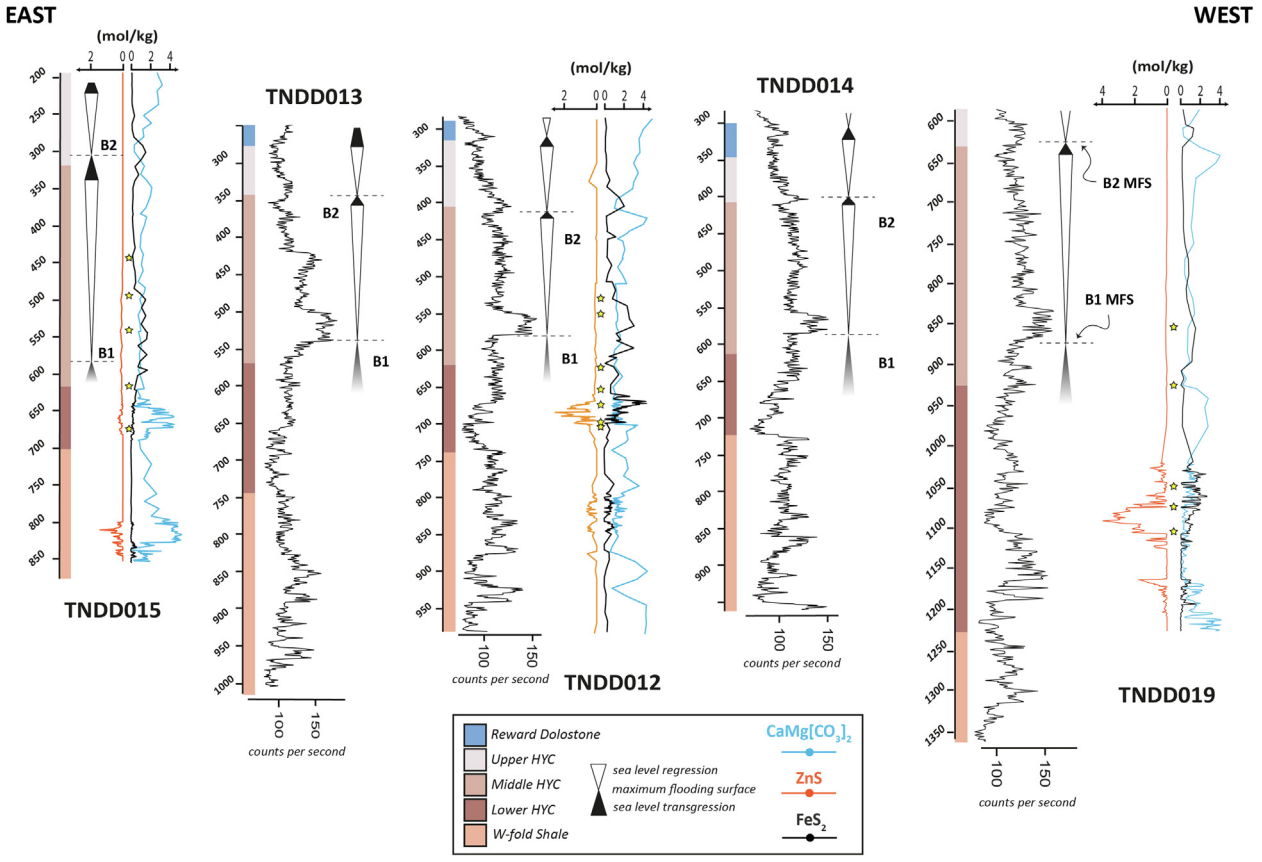

Fig. 4. Gamma response and chemostratigraphic logs for an east – west fence of 5 drill-holes. The chemical data show calculated abundances of sphalerite (orange), pyrite (black) and dolomite (blue) that were reported by Magnall et al., (2020). The yellow stars are the samples selected for LA-ICP-MS analysis. The main maximum flooding surfaces in the basin are labelled B1 and B2 and the respective underlying and overlying stratigraphic units were deposited during the main stages of transgressive and regressive sedimentation (modified after Magnall et al., 2021a).

of sphalerite postdate the formation of fine-grained diagenetic pyrite (py1a and py1b) and nodular dolomite, and are associated with two generations of pyrite (py2a and py2b). Sphalerite mineralization in the Lower and Main Lenses is considered to have formed primarily via dolomite replacement during burial diagenesis of the Lower HYC unit and broadly coeval with deposition of the overlying Middle HYC unit (Hayward et al., 2021; Magnall et al., 2021a).

3. METHODS

3.1. Samples

All samples were selected from drill-cores that intersected the bedded sulfide mineralization and the overlying hangingwall stratigraphy in the Teena subbasin (Figs. 2, 4). The samples that were selected for LA-ICP-MS analyses were previously analysed for sulfur isotopes in pyrite (Magnall et al., 2020) and were selected from 3 drill-holes (TNDD015, TNDD012 and TNDD019). The 3 drill-holes were chosen for a comparison of low- (TNDD015) and high-grade (TNDD012 and 019) Zn mineralization and to examine the pyrite in the hangingwall stratigraphy. Each sample was evaluated with the binocular microscope and thin sections were made for transmitted and reflected light microscopy, and further examined using scanning electron microscopy (SEM). Small (<4 mm diameter) pucks were drilled from thin section blocks using a diamond drill press and placed into an epoxy mount. The approach taken with sample preparation enabled the analysis of multiple samples from a broad stratigraphic interval in a single analytical session. A drill-core sample that preserves a high-angle sphalerite replacement interface was also selected for higher resolution micro sampling to compare the composition of pyrite formed either side of this boundary.

3.2. Lithogeochemistry

A suite of samples (n = 73) was selected to improve the spatial resolution of sampling in the hangingwall stratigraphy of the existing lithogeochemical dataset (Fig. 4; Magnall et al., 2021a, 2021b). Samples of half or quarter core (5 – 15 cm stratigraphic thickness) were sent to Bureau Veritas (Mt Isa) for major element and assay (Cu, Pb, Zn) analysis (XF01; oxidative fusion followed by XRF analysis). Trace elements were analysed via LA-ICP-MS of a fused glass disc following Li borate fusion digestion (LA001 analytical package). Carbon and sulfur were analyzed by LECO analysis. Blanks and certified reference materials (OREAS131a and 133a, AMIS) were submitted alongside the samples to monitor data quality.

3.3. EPMA

Representative examples of hydrothermal pyrite were analysed by wavelength dispersive spectroscopy (WDS) on polished mounted and carbon coated samples at the GeoForschungsZentrum (GFZ) Potsdam (Germany) using a field-emission JEOL Hyperprobe JXA 8500F. The conditions for the electron probe microanalyses conducted in the WDS mode included 15 keV, 20 nA and a 1 μm probe size. To determine elemental concentrations, calibration was done on certified natural and artificial sulfides and arsenides such as: pentlandite (Fe, Ni, S), sphalerite (Zn), galenite (Pb), stibnite (Sb), GaAs (As), and (Co, Ni)As_3 for Co. Counting times on the peak varied between 5 s for major and 30 s for TEs with corresponding backgrounds collected in half of the peak acquisition time. ZAF-Data correction for the interactions between incident electrons and the target (Z), between the generated photons and the matrix (A) and a fluorescence correction (F) was used. Under these conditions, detection limits are $\leq$ 0.02 wt.% for Fe, Ni, S, Co, As and 0.04 wt.% for Sb, and Zn and $\leq$ 0.07 wt.% for Pb.

3.4. LA-ICP-MS

Laser ablation ICP-MS analyses were carried out using the Analyte Excite 193 nm ArF* excimer-based laser ablation (LA) system (Teledyne Photon Machines, Bozeman, MT, USA), coupled to the quadrupole-ICP-MS iCAP from Thermo Scientific. The LA-system is equipped with a HelEx II 2-volume ablation cell. Helium was used as a carrier gas for aerosol transport from the sample surface to the ICP and was mixed downstream with Ar as a make-up gas before entering the plasma. Operational parameters of the ICP-MS instrument and LA-unit were tuned for maximum sensitivity, low oxide formation based on the $^{232}Th^{16}O/^{232}Th$ ratio and low laser-induced elemental fractionation based on the $^{238}U/\ ^{232}Th$ ratio using NIST SRM 610. Samples were ablated with a spot size of 10 μm for all pyrite analyses to ensure the necessary spatial resolution for targeting different paragenetic stages of pyrite and minimizing host rock contamination. Samples were ablated for 30 s with a repetition rate of 10 Hz and an energy density of 2–3 J/cm^2. The following isotopes were analysed: ^{55}Mn, ^{57}Fe, ^{59}Co, ^{60}Ni, ^{63}Cu, ^{66}Zn, ^{72}Ge, ^{75}As, ^{77}Se, ^{98}Mo, ^{109}Ag, ^{121}Sb, and ^{208}Pb. The time intervals for data reduction were selected by visual inspection of each spectrum using Iolite™ (Paton et al., 2011) and elemental concentration are calculated using the data reduction scheme X_trace_elements_IS (Longerich et al., 1996). We used ^{57}Fe as internal standard and the reference materials MASS-1 (USGS) and UQAC-FeS1 (Kiel). The UQAC standard was used as the primary reference material for Co, Ni, Mo and Ag, as it produced more accurate data when using the MASS-1 reference material as a secondary standard. All other elements were quantified using MASS-1 as the primary reference material and UQAC as the secondary standard.

During data processing several measures were taken to monitor data quality. Owing to the complex zonation and the multi-stage paragenesis of the hydrothermal sulfides, many of the analyses were mixed ablations that included non-pyrite phases. Careful visual evaluation of each analysis was required in order to select the time series over which only pyrite was ablated (e.g. Fig. 5). The error associated with each analysis provided a useful indication of the potential for mixed ablation signals and analyses where the standard error (2σ) exceeded 50% of the overall signal

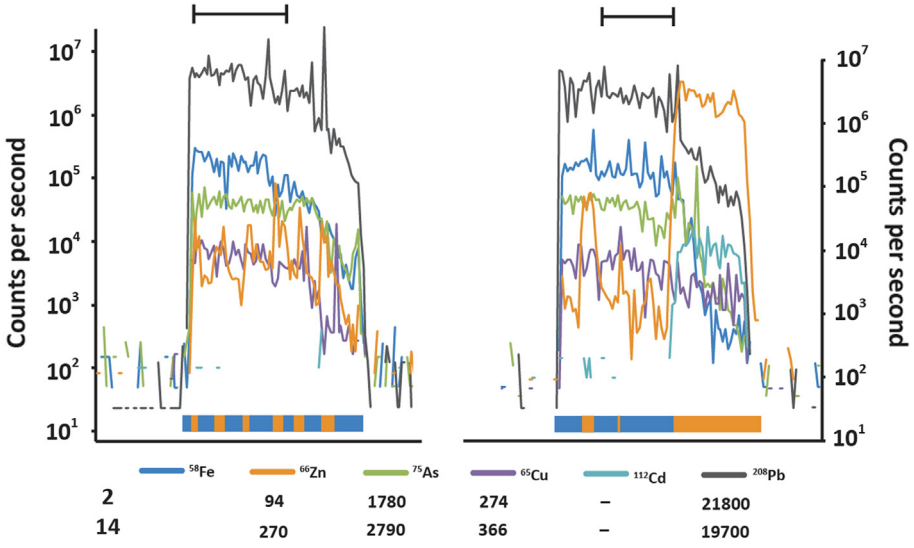

Fig. 5. The counts per second profiles for two LA-ICP-MS ablations of py2 from the sample shown in Fig. 9F. The colours represent the different elements and the horizontal bars at the top represent the areas selected for data integration. The horizontal-coloured bars at the bottom represent the main mineral phase that was ablated. The second profile shows a major increase in Zn during the latter stage of the ablation, indicating that sphalerite was the main phase during this stage of the ablation.

were highlighted for further scrutiny. In general, a good correlation between Zn and Cd at relatively high signals (counts per second) was consistent with the ablation of sphalerite rather than pyrite. Additional steps for evaluating data quality included: (1) a comparison between data generated by EPMA and LAICPMS in a subset of samples; (2) a comparison of analyses of py1 that was contained in different host rock matrices (dolomite nodules vs. organic rich matrix) to evaluate host rock contamination, and; (3) an evaluation of the mass balance of TEs in pyrite relative to bulk rock concentrations.

3.5. Principal Component Analysis

The dimensionality of the pyrite TE dataset was reduced using principal component analysis (PCA) with the computer software package ioGAS. As with other multivariate datasets, a log transformation of each variable was used to ensure positively skewed distributions did not effect trends present in the bulk of the dataset (Reimann et al., 2008). The Robust M−estimation function was used, which attributes outliers with a low weighting so that they are effectively ignored in the correlation matrix. Imputation of a fixed value (0.5 * LOD) was carried out to minimize the loss of data that resulted from incomplete analyses (i.e. samples containing some elements below LOD). Prior to imputation, data loss for each individual element was mostly on the order of $< 5\%$ (apart from Ge) and accounted for 12% of the dataset.

4. RESULTS

4.1. Petrography

The two most volumetrically important stages of pyrite formation in the Teena subbasin comprise: (1) aggregates of diagenetic, microcrystalline (<5 μm) euhedral crystals that are concentrated along irregular carbonaceous laminations (py1a; Fig. 6A) and slightly larger (>5 μm) idiomorphic crystals that occur within or at the margins of dolomite nodules (py1b; Fig. 6B). (2) Hydrothermal pyrite that formed during the main stage of Zn mineralization in the Lower HYC unit can be subdivided into: (i) py2a, which forms variably sized (≥10 μm) spherical crystals (py2a) that sometimes preserve colloform growth textures and high intracrystalline porosity (e.g. Fig. 6C and 7); (ii) py2b, which is typically an inclusion free anhedral overgrowth of earlier formed py1a and py2a with occasional fine-scale sector zonation (e.g. Figs. 6, 7 and 8), and; (3) py2c, which is volumetrically minor and forms fibrous overgrowths on py2b that infill pore space in an assemblage with sphalerite (e.g. Fig. 6H). It can be difficult to differentiate between py2a and py2b, but in general py2a tends to be more porous relative to more crystalline aggregates of py2b. A drill-core sample that shows fine-grained sphalerite cement crosscutting sedimentary layering in the pyritic mudstone is an important example of the paragenetic relationship between sphalerite and py2 (Fig. 9). The volumetrically minor py2c generation is associated with late-stage stratiform replacement bands and vug-fill of coarse-grained sphalerite, galena and pyrite in the higher-grade main mineralized lens.

The final stage of pyrite (py-vein) is restricted to late stage synorogenic sulfide veins that formed from remobilization of sphalerite and galena from the surrounding host rock (Hayward et al., 2021). There are also multiple generations of pyrite in the footwall mineralization lenses hosted by the W-Fold Shale Member (described in Hayward et al., 2021), but the focus of this study is the higher-grade mineralization in the Lower HYC unit and the overlying hangingwall sequence.

4.2. Bulk rock geochemistry

A number of TEs (Mo, V, Co and Ni) all covary with total organic carbon (TOC) in samples from the Middle and Upper HYC units (Fig. 10). The samples from the Middle HYC unit preserve higher concentrations of Mo and V relative to those from the Upper HYC unit. Samples from the pyritic interval overlying the B1 maximum flooding surface that contain high TOC concentrations (>2.5 wt.%) plot away from the trend that defines the remainder of the Middle HYC unit and towards lower TOC normalized values that are more similar to samples from the Upper HYC unit (Fig. 10A). Samples from this interval (>2.5 wt.% TOC) also have high molar TOC/P ratios (Fig. 10B) that

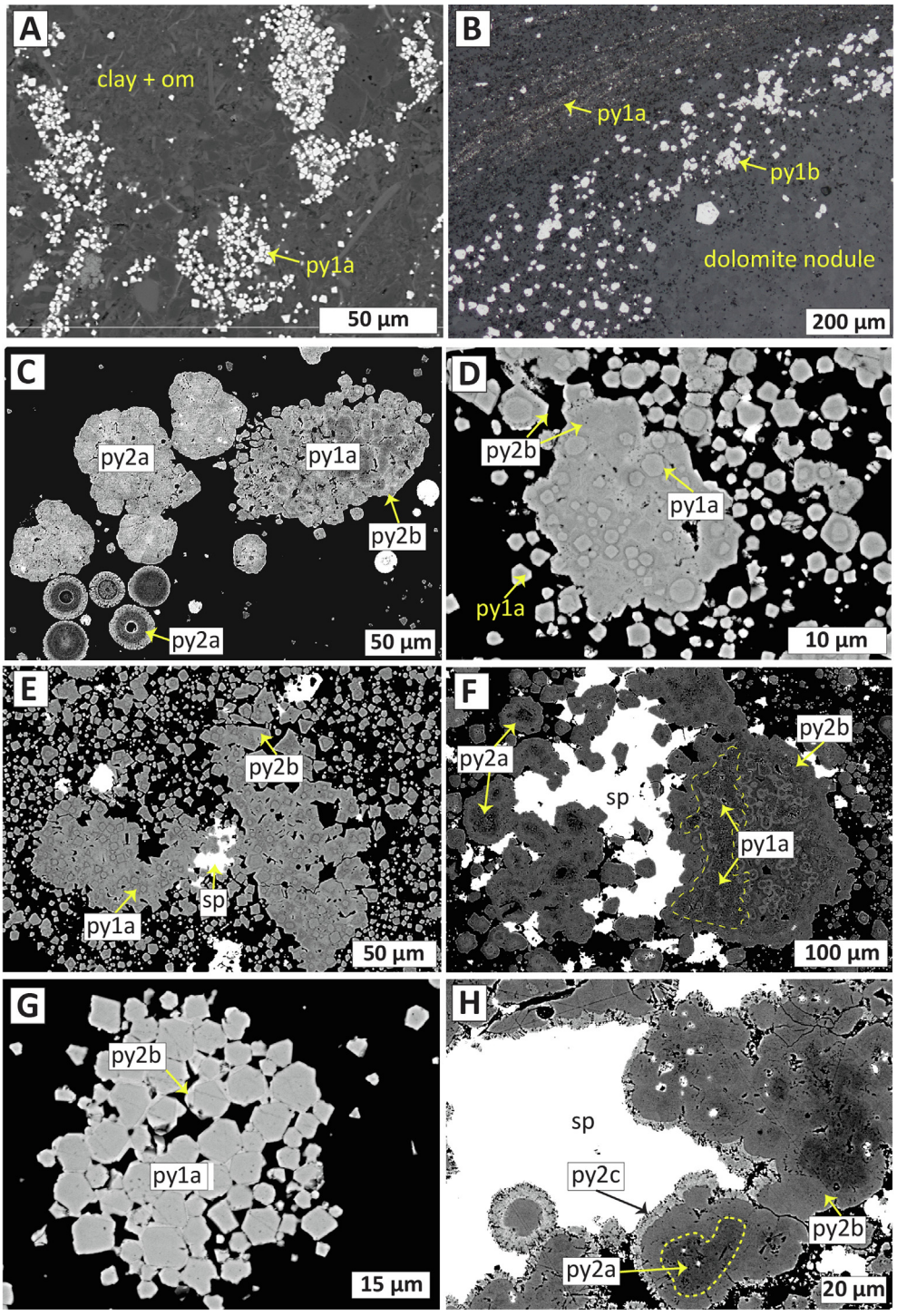

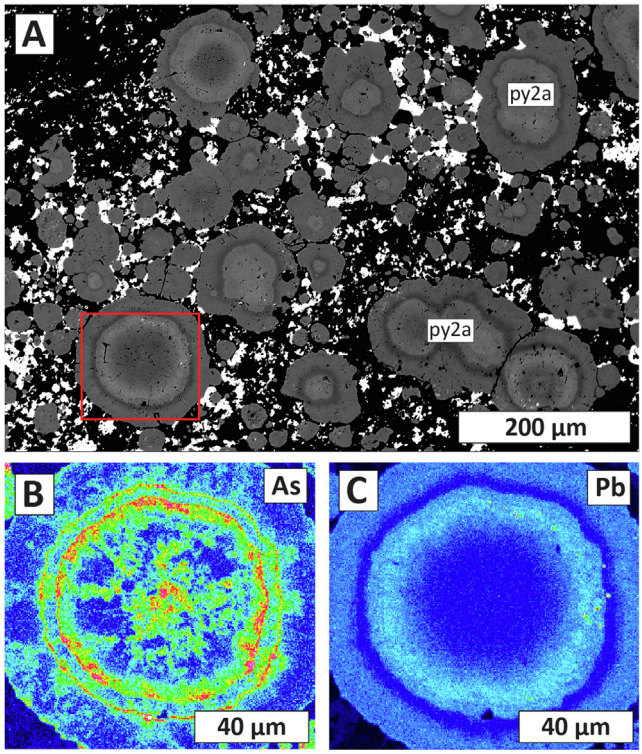

Fig. 7. (A) A backscatter electron image of spherically zoned crystals of py2a that are overgrown by anhedral py2b. The white phase which forms fine-grained interstitial disseminations is sphalerite that formed mostly by replacement of matrix dolomite. (B) A wavelength dispersive spectroscopy (WDS) compositional image of As showing the spherical zonation and radiaxial structure of the py2a crystals. (C) A WDS compositional image for Pb of the same area shown in (B).

correspond with highly positive $\delta^{34}S$ values (Magnall et al., 2020). As other sulfide phases have not been identified in the petrographic study of the un-mineralised Middle and Upper HYC units, the concentration (mol/kg) of pyrite can be calculated from total S (i.e. $FeS_2 = 0.5 * (\text{total S} - (\text{Pb} + \text{Zn}))$. All bulk rock data are available in a supplementary data file (Magnall et al., 2021b).

4.3. Pyrite chemistry (LA-ICP-MS and EPMA)

A total of 1262 sample ablations were produced on 17 samples that were selected from the Lower and Middle HYC units (Fig. 4). In the Upper HYC unit, the concentrations of py1a are lower relative to the Lower and Middle HYC units and there are fewer concentrated aggregates of py1a that were amenable to *in situ* analyses. The fine-grained nature of the samples and complex intergrowths between sulfide phases meant that uniform ablation profiles were the exception rather than the rule. Ablations that contained an unacceptable fraction of host rock or sphalerite were removed from the dataset (n = 460 analyses). The majority of remaining analyses were of py1a and py2 (a + b), which are volumetrically the most important in the respective units. A number of analyses (n = 49) also rep-

Fig. 6. Petrographic examples of diagenetic (py1) and hydrothermal (py2) generations of pyrite. All are backscatter electron images apart from B, which was taken in reflected light. (A) Aggregates of micro-euhedral pyrite (py1a) within the carbonaceous mudstone of the Middle HYC unit (JM132 @ 548 m in TNDD015). The matrix comprises a mixture of amorphous organic material and clay minerals. (B) Py1a in the carbonaceous matrix surrounding a dolomite nodule, which contains coarser grained py1b within its outer margin (JM63 @ 1181 m in TNDD019). (C) Fine-grained py1a overgrown by hydrothermal pyrite (py2). A range of morphologies are typical of py2a, which in this example has formed individual spherically-zoned crystals and more anhedral recrystallized aggregates; py2b has formed anhedral overgrowths to py1a. (JM78 @ 1069 m in TNDD019). (D) Subhedral to euhedral overgrowths of py2b on py1a (JM78 @ 1069 m in TNDD019). (E) Euhedral overgrowths of py2b on py1a together with minor interstitial sphalerite (JM78 @ 1069 m in TNDD019). (F) The porous cores of py2a that are overgrown by py2b among interstitial sphalerite. The yellow dashed lines marks a relict aggregate of py1a crystals. (JM156 @ 671 m in TNDD012). (G) Very minor overgrowths of py2b among a spherical aggregate of py1a crystals (JM78 @ 1069 m in TNDD019). (H) Multiple stages of pyrite formation in the high-angle replacement sample (see Fig. 9). The yellow dashed line outlines a core of porous py2a that has been overgrown by py2b; py2c forms a cavity-lining fibrous overgrowth on py2b and is associated with infilling coarse-grained sphalerite.

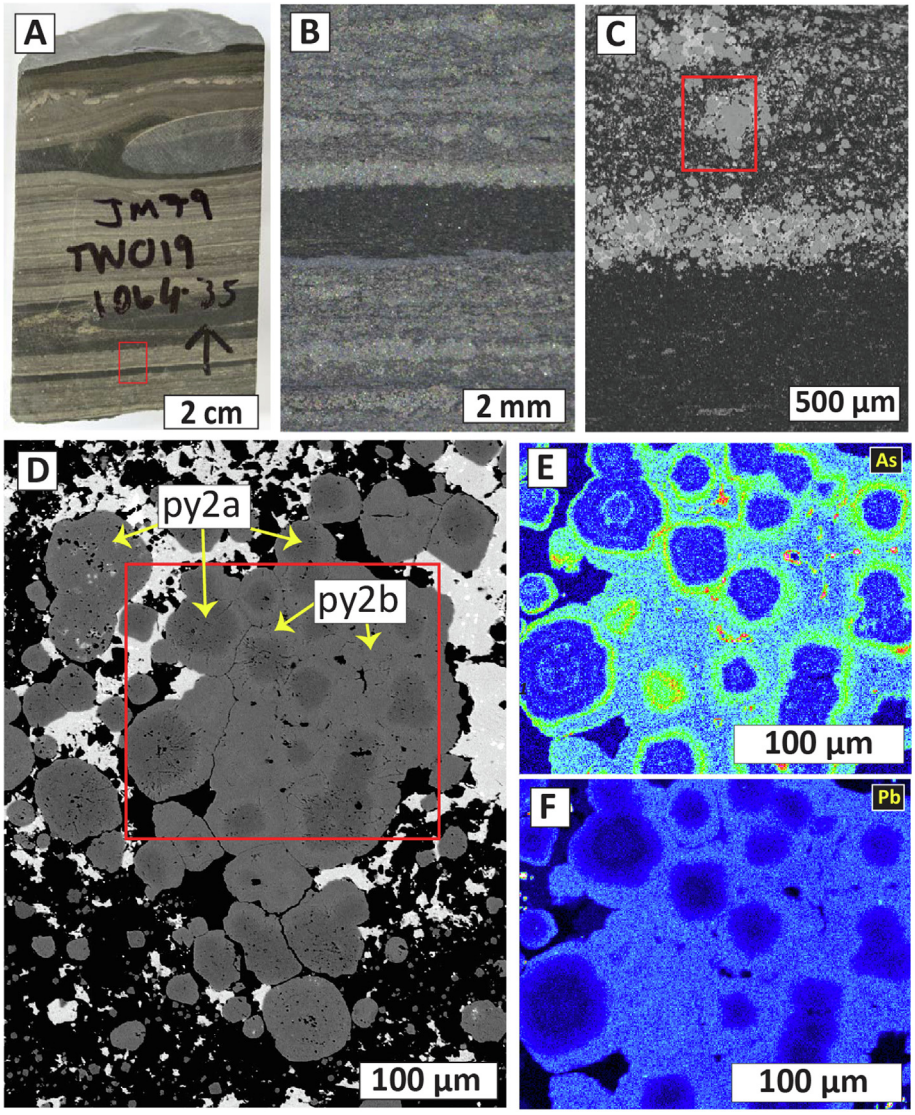

Fig. 8. (A) Hand sample of the mineralization in TNDD019 (JM79 at 1064 m). The red box highlights the area shown in B. (B) A binocular microscope image of a carbonaceous mudstone lamination associated with stratiform pyrite. The pyritic laminations that comprise most of the image are cemented by fine-grained sphalerite. (C) A backscatter electron (BSE) image showing the interface between the stratiform pyrite and carbonaceous mudstone lamination shown in B. (D) A higher resolution BSE image of the area shown in C, in which there is an aggregate of py2a that has been overgrown by py2b. Red box marks the area shown in E and F. (E) and (F) WDS compositional images showing the distribution of As (E) and Pb (F) in the area shown in D.

resent mixed ablations of py1a and py2b, as the 2 subtypes are intergrown. Analyses of py1b were restricted to a small number (n = 5).

The LA-ICP-MS data are available in a supplementary datafile (Magnall et al., 2021c) and a summary of the results is presented in Table 1 (grouped by pyrite generation). Median compositions of the Teena pyrite are compared with median compositions of diagenetic pyrite from the McArthur Basin (Fig. 11A), a broader compilation of diagenetic pyrite from Proterozoic marine sedimentary rocks (Fig. 11B), and SEDEX pyrite (Fig. 11C). Relative to diagenetic pyrite from the McArthur Basin and Proterozoic datasets, py1a from the Teena subbasin is strongly enriched in Tl, and moderately enriched in Zn, Pb and As (Figs. 11A and B). The median composition of py1a from the Middle HYC unit is also strongly enriched in Zn and Pb compared to py1a from the Lower HYC unit (Figs. 11A and B). There is a better correlation between the Mo, Co, and Ni composition of py1a from the Middle HYC unit and analyses of diagenetic pyrite from the McArthur Basin.

There is no major difference in the TE composition of the 2 major subtypes of py2 (Fig. 11C). Notably, there is also very little change in the TE composition of py2 either side of the interface between sphalerite mineralization and un-mineralized host rock in the sample shown in Fig. 9. The only minor exception is Cu, which has slightly lower

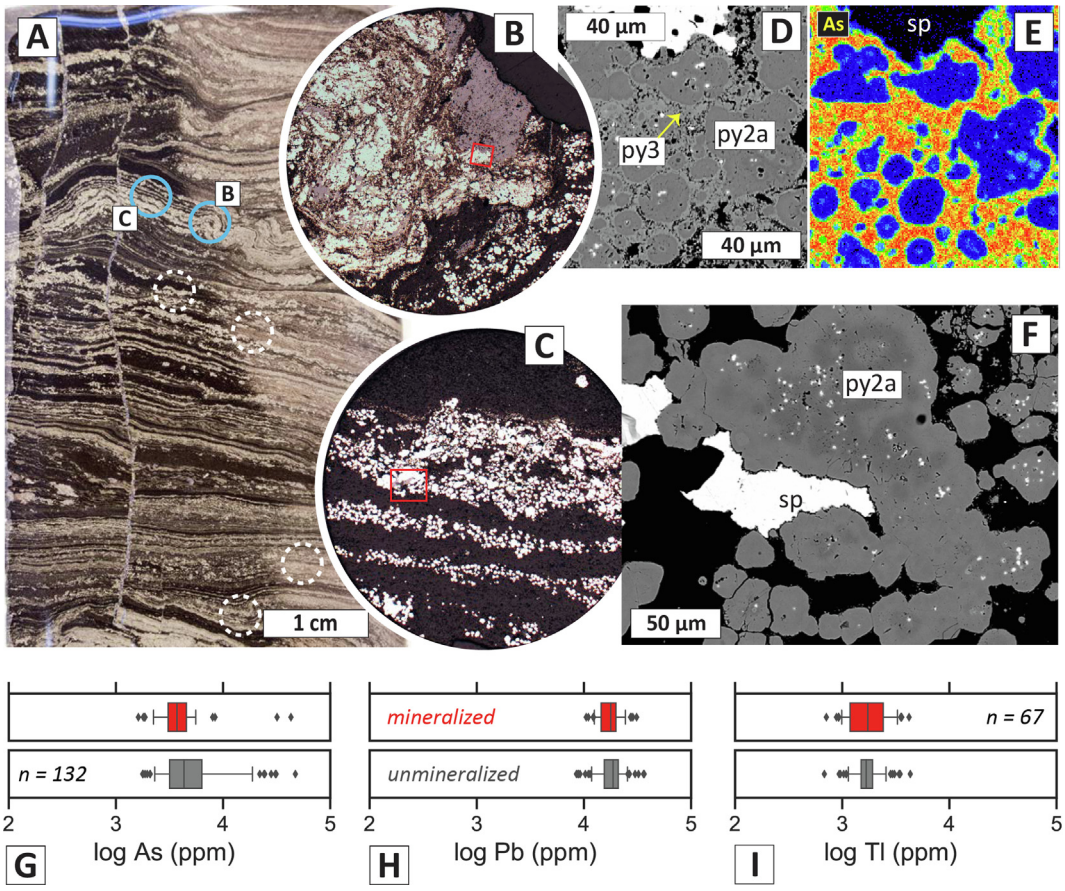

Fig. 9. (A) Hand sample photograph of a wet drill-core sample (TNDD025 @ 730 m) showing the interface between pyritic carbonaceous mudstone (left) and a fine-grained sphalerite replacement front (from right). The sub-samples drilled out for further microscopy and LA-ICP-MS are highlighted by the blue and dashed white circles. (B) Reflected light image of a sub-sample from A, showing a large aggregate of py2 intergrown with sphalerite. The red box marks the area shown in D and E. (C) Reflected light image of a sub-sample from A, showing stratiform crystals of diagenetic py1 and hydrothermal py2. The red box marks the area show in F. (D) A backscatter electron (BSE) image showing the area in B (red box) where py2a has been cemented by later py2c growth. (E) WDS compositional image showing the As distribution in the same image as D (warm colours = higher concentrations). (F) A backscatter electron image showing a porous aggregate of py2a that contains inclusions of sphalerite (sp) and is overgrown by py2b. (G) A boxplot showing As (log ppm) in py2 in the Zn mineralized (red) and unmineralized (grey) half of the sample (H) A boxplot showing Pb (log ppm) in py2 in the Zn mineralized (red) and unmineralized (grey) half of the sample (I) A boxplot showing Tl (log ppm) in py2 in the Zn mineralized (red) and unmineralized (grey) half of the sample. The whiskers in the boxplots (G to I) extend to the 5th and 95th percentiles and boxes define the interquartile range.

concentrations on the unmineralized side of the sample. Relative to the median composition of SEDEX pyrite, the median composition of py2 is strongly enriched in Tl (by almost 2 orders of magnitude) and Pb, moderately enriched in As, and depleted in Mo, Co, Ni, and Sb (Fig. 11C). The analyses that represent mixed ablations of py1a and 2b contain Mo concentrations that are closer to the end-member analyses of py1a. Analyses of coarse-grained pyrite in the late stage veins contain the highest concentrations of Ag, but are notably depleted in As and Tl (Table 1).

Element mapping by WDS provides evidence of major grain scale compositional variability in py2, with micron scale sector style zonation in As and Pb (e.g. Figs. 7, 8, and 9). In Fig. 12, the Fe and S concentrations (mol.%) from WDS spot analyses are plotted against As + Pb (mol.%) and there is a moderate negative correlation with Fe but no correlation between S.

4.4. Degree of trace metal pyritization

The degree of trace metal pyritization (DTMP) has been calculated from the median concentrations of py1a and corresponding total pyrite and trace metal (X) in the whole rock (wr):

Degree of trace metal (X) pyritization (%) = (pyrite_{wr} * X_{pyrite})/X_{wr}

A summary of the data is provided in Table 2 and Fig. 13. In samples from the Middle and Lower HYC units the DTMP of Mn is low (<40%). The DTMP of all other trace metals is generally higher than 40%, although there is considerable variability between samples. Pyrite contains between 50 and 98% of the whole rock budget of Co and Ni, and results are consistent between samples from the Lower and Middle HYC units. A large proportion of Mo (56 to 101%) and Pb (42 to 97%) is associated with pyrite

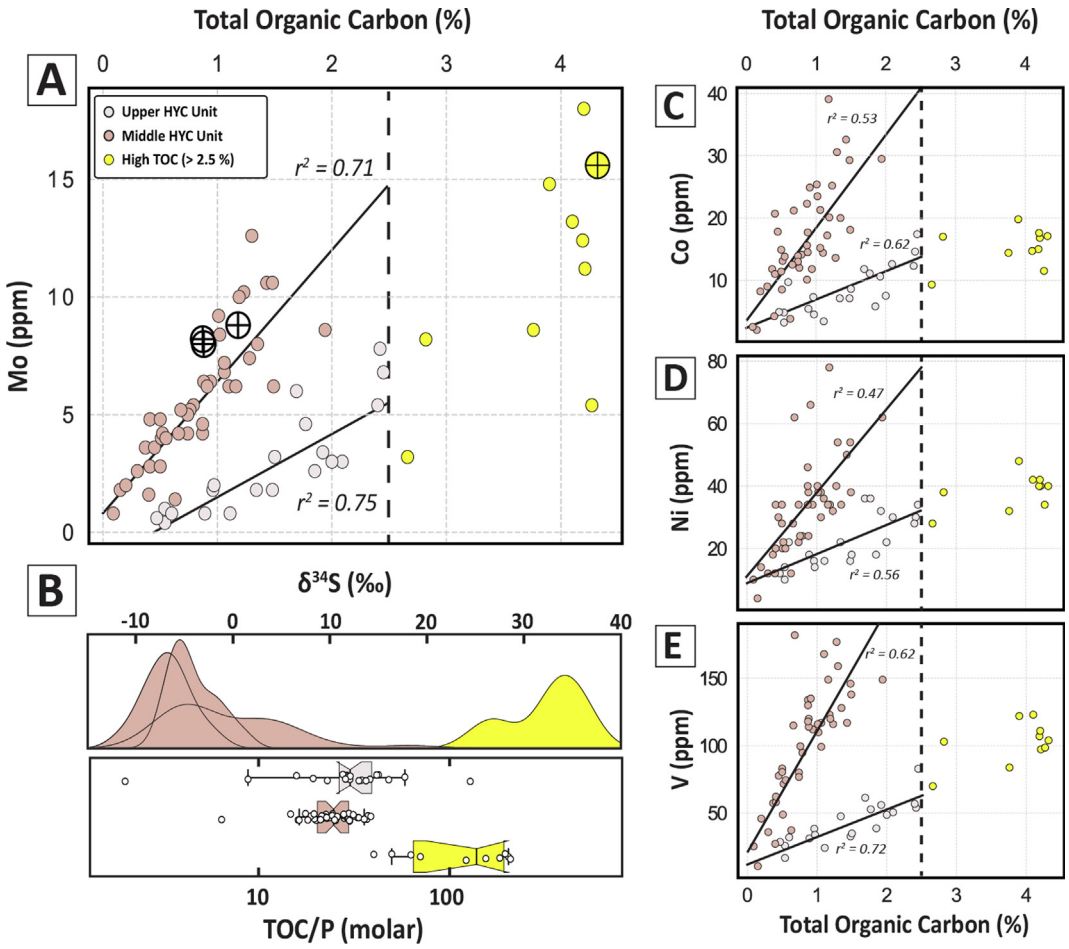

Fig. 10. (A) Total organic carbon (TOC; wt.%) vs. Mo (ppm) in the Middle and Upper HYC units. The large crossed-circle symbols are samples from which *in situ* $\delta^{34}S$ values in pyrite have been produced (Magnall et al., 2020). (B) Probability density functions for $\delta^{34}S$ values in pyrite and boxplots for the TOC/P (molar) of samples from the Middle and Upper HYC units. (C) TOC (wt.%) vs. Co (ppm). (D) TOC (wt.%) vs. Ni (ppm). (E) TOC (wt.%) vs. V (ppm).

in samples from the Middle HYC unit, although it is much lower in the two samples from the Lower HYC unit (Mo = 18 to 21% and Pb = 2 to 6%). There is much greater variability in the DTMP of the remaining metals in pyrite, including notable outliers for Zn and Ag (>200%), and Cu, As, Tl, and Ge (>100%).

4.5. Principal component analysis and literature comparison

The first two principal components describe almost 60% of the total variance in the pyrite chemistry dataset (Fig. 14A). There are three main element groupings in a plot of PC1 vs. PC2, which differentiate between diagenetic (black; negative PC1) and the main hydrothermal event (red; positive PC1). The As and Cu grouping is associated with the small number of py-vein analyses and is not considered important. The relationship between the diagenetic and hydrothermal end members can also be presented as an element ratio that includes those elements that preserve the most variance (Mo, Ni, Tl, As, Pb; Fig. 14C). The (Tl + As + Pb)/(Mo + Ni) ratio is effective for differentiating between the different paragenetic stages of pyrite in the Teena subbasin. The mixed ablations (py1a/2b) preserve compositions that are intermediate between the diagenetic and hydrothermal end members (Fig. 14C). In terms of spatial trends, when separated by stratigraphic unit, the ratio values show approximately uniform compositions in TNDD015, whereas there is a systematic increase in values down towards the main (upper lens) mineralization interval in samples from TNDD012 and 019 (Fig. 15). In the sample with the replacement front, the index values for pyrite are relatively uniform and overlap analyses of py2 from other samples in the Lower HYC unit (Fig. 15).

The (Tl + As + Pb)/(Mo + Ni) ratio has also been calculated for a compilation of pyrite chemistry generated on Proterozoic samples from different sedimentary basins (Large et al., 2014; Mukherjee and Large, 2017), which are presented as a series of probability density functions that show the distribution of different subgroups (Fig. 16). The broader dataset of Proterozoic data has been filtered for samples from the McArthur Basin, which preserve slightly higher ratio values (median = 5.3 vs. median = 1.2). The ratio values for py1a and py2 in the Teena subbasin are higher again, with median values of 30.2 and 883.4 respec-

Table 1
Summary table of LA-ICP-MS results. Limit of detection = LOD and median absolute deviation = MAD.

		Lower HYC			*Middle HYC*											
		py1a			**py1a**			**py1a/py2b**			**py2a**			**py2b**			**py3**		
Element (ppm)	mean LOD	*n*	median	MAD	*n*	median	MAD	*n*	median	MAD	*n*	median	MAD	*n*	median	MAD	*n*	median	MAD
Mn	4.2	*57*	278.0	198.0	*126*	1040.0	544.0	*97*	357.0	213.0	*286*	94.0	43.1	*121*	98.0	42.0	*17*	500.0	491.7
Co	0.9	*57*	27.1	19.5	*126*	88.5	25.5	*97*	3.6	2.5	*286*	18.9	11.5	*121*	15.3	10.4	*17*	0.5	0.3
Ni	6.9	*57*	87.0	53.0	*126*	246.5	70.0	*97*	17.6	10.5	*286*	24.8	11.2	*121*	22.9	12.2	*17*	1.0	0.0
Cu	8.5	*57*	271.0	83.0	*126*	299.5	100.0	*97*	292.0	155.0	*286*	278.0	132.5	*121*	224.0	111.0	*17*	282.0	167.0
Zn	22.4	*57*	87.0	33.0	*126*	10150.0	9785.5	*97*	270.0	236.0	*286*	88.0	55.5	*121*	102.0	67.0	*17*	18.0	10.0
Ge	5.0	*57*	8.4	2.7	*126*	7.4	6.4	*97*	9.1	1.6	*286*	8.3	1.2	*121*	8.8	1.2	*17*	8.3	1.0
As	26.8	*57*	2820.0	990.0	*126*	2110.0	615.0	*97*	4340.0	1940.0	*286*	3820.0	1040.0	*121*	3860.0	1150.0	*17*	52.0	47.3
Mo	0.3	*57*	20.2	10.7	*126*	54.0	21.1	*97*	21.5	10.8	*286*	1.5	0.7	*121*	1.3	0.7	*5*	1.8	1.3
Ag	1.1	*57*	6.8	2.9	*126*	10.3	4.6	*97*	4.9	4.7	*286*	7.2	3.1	*121*	5.4	2.9	*17*	42.0	20.0
Sb	3.0	*57*	98.0	60.0	*126*	101.0	36.5	*97*	20.7	13.1	*286*	5.8	4.3	*121*	7.3	6.1	*17*	77.0	70.3
Tl	0.1	*57*	445.0	195.0	*126*	274.0	101.5	*97*	790.0	370.0	*286*	1840.0	360.0	*121*	1800.0	450.0	*17*	5.6	4.4
Pb	0.7	*57*	890.0	460.0	*126*	4125.0	2250.0	*97*	1100.0	737.0	*286*	18300.0	3200.0	*121*	18000.0	3000.0	*17*	4410.0	3020.0

tively. The interquartile range of each subgroup of data covers approximately one order of magnitude.

5. DISCUSSION

The sulfide mineralization in the Teena subbasin formed via host rock replacement during burial diagenesis and has a complex paragenesis (Hayward et al., 2021). As a result, the trace element (TE) composition of the Barney Creek Formation (BCF) will have been affected by a combination of biogenic, authigenic, and hydrothermal processes. The first part of the discussion will focus on using relationships between TEs and TOC in the bulk rock data to determine the primary controls on biogenic and authigenic TE enrichment in the Middle HYC unit. The pyrite chemistry dataset has then been used to evaluate the TEs associated with hydrothermal activity in the Lower HYC unit and the nature of TE dispersion around the Teena mineral system. Both of these themes have broad implications for paleoenvironmental reconstructions in the Proterozoic and understanding how metals are hydrothermally dispersed around subseafloor sediment hosted mineral systems.

5.1. Constraints on depositional paleoredox and subbasin redox architecture (TOC, P, and TEs)

The systematic trends between TOC, P and a number of TEs (Fig. 10) are consistent with the interplay of subbasin hydrography, primary productivity, and depositional paleoredox conditions (e.g. Algeo and Lyons, 2006). As a limiting nutrient to primary productivity in marine environments, the availability of P would have perhaps provided the most important constraint on depositional redox conditions in the Teena subbasin (e.g. Ingall et al., 1993; Tyrrell, 1999). In marine sediments, the majority of P is associated with organic matter and Fe (oxyhydr)oxides (Algeo and Ingall, 2007), and as depositional redox conditions become more reducing, the regeneration of P from organic matter and oxide phases is enhanced (e.g. Slomp et al., 2004; Van Cappellen and Ingall, 1994). Phosphorus regeneration is particularly high under euxinic conditions, where the TOC/P ratio commonly exceeds the reference value for phytoplankton in modern marine environments (~106:1; Redfield, 1958). In the Proterozoic oceans, nutrient limitation (oligotrophy) could have resulted in TOC/P ratios in organic matter that exceeded the canonical Redfield ratio (e.g. Reinhard et al., 2017). Despite this uncertainty, it is still possible to obtain information from stratigraphic variability in TOC/P ratios when coupled with additional geochemical data. For example, the highest TOC/P ratios correspond with samples from the interval overlying the B1 MFS in the Teena subbasin (Figs. 4, 10B), where there are also high concentrations of diagenetic pyrite with highly positive $\delta^{34}S$ values (Fig. 10B). This pyrite from above the B1 MFS formed under sulfate-limited euxinic conditions (Magnall et al., 2020), which is consistent with the high TOC/P ratios that indicate P regeneration (e.g. März et al., 2008).

In the Teena subbasin, the degree of TE enrichment relative to TOC is highest for samples from the Middle

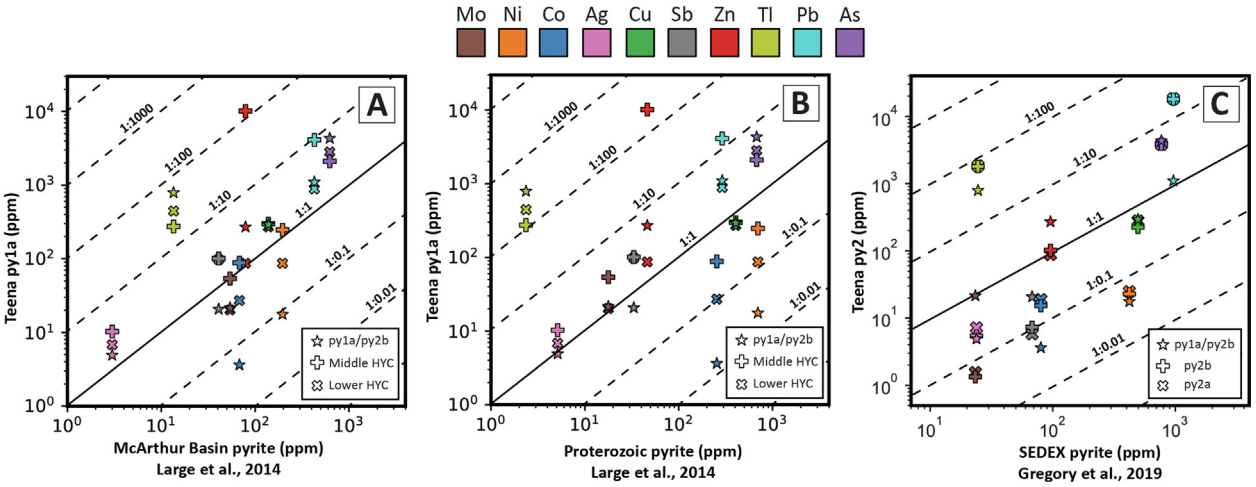

Fig. 11. (A) A comparison between the median composition of diagenetic pyrite analyses from the McArthur Basin (Large et al., 2014) and the median composition of py1a (subdivided by stratigraphic unit; Lower and Middle HYC unit) and mixed ablations of py1a and py2b. (B) A comparison between the median composition of a compilation of pyrite analyses from the Proterozoic (Large et al., 2014) and the median composition of py1a (subdivided by stratigraphic unit; Lower and Middle HYC unit) and mixed ablations of py1a and py2b. (C) A comparison between median composition of SEDEX pyrite (Gregory et al., 2019) and the median composition of py2a, py2b, and mixed ablations of py1a and py2b.

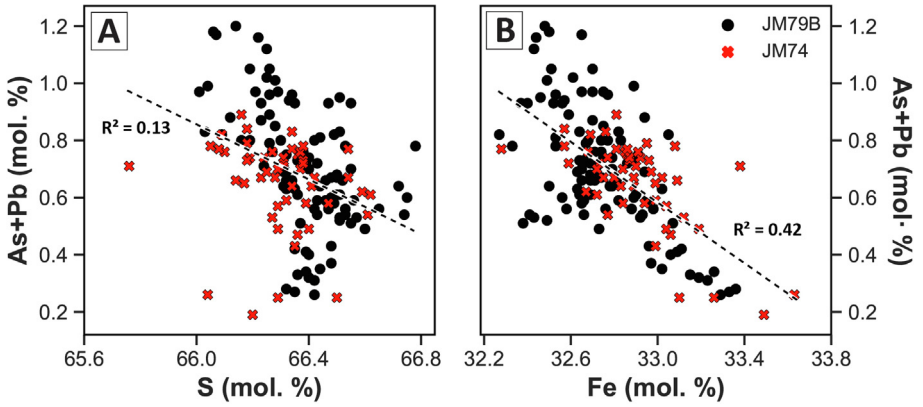

Fig. 12. (A) A bivariate plot of S (mol.%) vs. As + Pb (mol.%) in py2. (B) A bivariate plot of Fe (mol.%) vs. As + Pb (mol.%) in py2.

HYC unit (Fig. 10A, C, D and E), which contains facies deposited at the peak of subbasin deepening (Hayward et al., 2021). The highest levels of TE enrichment, therefore, developed when there would have been maximum connectivity to the surrounding regional water mass, thereby allowing for TE replenishment into the subbasin (Algeo and Lyons, 2006). In contrast, the Upper HYC unit was deposited during the regressive cycle, which is characterised by a transition from slope and subtidal facies to more subtidal and intertidal facies (Hayward et al., 2021). The TOC concentrations in the Middle and Upper HYC units are comparable (Fig. 10), meaning the decrease in TE abundance in samples from the Upper HYC unit likely corresponds with limited TE replenishment under restricted hydrographic conditions rather than dilution related to higher sedimentation rates (Liu and Algeo, 2020).

There is a TOC threshold (2.5 wt.%) above which the covariation with TEs breaks down (e.g. Fig. 10A), which is limited to the samples from the euxinic interval overlying the B1 MFS (Fig. 4). A similar breakdown in TE-TOC covariation has been described in other Proterozoic sequences (Cox et al., 2016; Johnston et al., 2010) and can be explained by the stronger relationship between TEs and water column sulfide under euxinic conditions (Algeo and Maynard, 2004). The overall abundance of Mo in the euxinic interval is low (<17 ppm; Fig. 10A) when compared with other Proterozoic units deposited under euxinic conditions (e.g. Reinhard et al., 2013). A decline in authigenic Mo enrichment during the mid-Proterozoic has been linked with low atmospheric O_2 and a smaller oxidative weathering flux to the oceans (Scott et al., 2008), although samples from this time period are limited to a small number of localities. If Mo concentrations in mid-Proterozoic seawater were lower they would have been more susceptible to reservoir effects, which were likely controlled by a combination of subbasin hydrography and euxinia during the BCF depositional cycle.

Table 2
The concentration of TEs in whole rock and median concentrations for LA-ICP-MS analyses of pyrite.

		Bulk rock composition						Median pyrite composition (LAICPMS)						
		Middle HYC unit				*Lower HYC unit*		*Middle HYC unit*				*Lower HYC unit*	
		JM132	JM136	JM163	JM165	JM159	JM158	JM132	JM136	JM163	JM165	JM159	JM158
Pyrite	wt. %	11.5	19.1	19.0	17.2	7.0	4.9	n 17	41	19	10	6	10
Mo	ppm	8.2	15.6	12.4	8.8	8.0	4.6	ppm 56	46	60	52	21	20
As	ppm	209.0	361.0	431.0	289.0	343.0	345.0	ppm 1385	2550	1670	1970	1485	2235
Co	ppm	22.3	17.1	15.0	39.1	14.5	14.6	ppm 121	63	69	114	115	215
Cu	ppm	68.0	52.0	48.0	50.0	82.0	164.0	ppm 440	229	300	389	166	205
Ni	ppm	40.0	40.0	40.0	78.0	38.0	46.0	ppm 259	140	207	308	460	550
Tl	ppm	20.6	50.4	53.4	55.4	25.6	26.2	ppm 106	346	238	410	320	226
Pb	ppm	940.0	1590.0	1630.0	1400.0	1320.0	2210.0	ppm 3450	4100	5700	7900	1150	805
Zn	ppm	3650.0	10600.0	6850.0	7880.0	6570.0	9460.0	ppm 23650	12000	77000	64500	530	390
Ge	ppm	2.1	2.6	2.2	2.0	2.3	4.9	ppm 11	*1*	*1*	17	*1*	*1*
Mn	ppm	700.0	1200.0	800.0	500.0	900.0	600.0	ppm 236	1290	1540	860	546	58
Ag	ppm	1.6	1.0	1.5	1.1	1.4	2.1	ppm 13	8	16	18	4	8
Sb	ppm	22.6	15.0	17.6	19.5	25.4	40.4	ppm 145	84	74	129	91	183

The closest modern analogue for the BCF is found in the Baltic Sea, which is the best example of a large, intracontinental basin that is characterized by extensive anoxic conditions (Algeo et al., 2008). In the Baltic Sea, topographic and hydrographic factors have resulted in strong gradients in water chemistry that are controlled by estuarine circulation rather than the upwelling and offshore currents that are typical of open marine continental margins (e.g. Fig. 3A, B). The geographical extent of the Baltic Sea (0.42×10^6 km^2; Algeo et al., 2008) is similar to the McArthur Basin (outcrop extent of 0.2×10^6 km^2; Allen et al., 2015) and the sedimentary record in both settings preserves a complex history of paleoenvironments and water depth. For example, in both settings there has been a progression from a freshwater lake to brackish marginal marine, through to a fully marine environment (Algeo et al., 2008). Similar to the depositional environment of the BCF, the modern-day Baltic Sea is also predominantly shallow marine with a small component of deeper water topographic depressions where euxinic conditions develop (Scholz et al., 2013; van de Velde et al., 2020a).

Considering the role of paleo-highs and subbasin depocenters in controlling facies variability in the BCF (Kunzmann et al., 2019; Blaikie and Kunzmann, 2020), paleoenvironmental reconstructions of the McArthur Basin might better resemble a silled basin model in which there were varying degrees of connectivity with the open ocean (e.g. Fig. 3C). In this model, contradictory proxy records may simply be a function of lateral facies variability that are typical of intracontinental basins. For example, the observation that biomarkers in modern lacustrine settings are similar to those described in the McArthur Basin could be the result of depositional transport from adjacent facies, rather than being a fundamental discrepancy in the broader depositional environment (c.f. French et al., 2020). Similarly, the evidence of ferruginous depositional redox conditions (Planavsky et al., 2011) versus the presence of sulfide in the photic zone (Brocks et al., 2005) need not be mutually exclusive. Sequence stratigraphy has considerable potential to augment the interpretation of lithogeochemical data in these settings (LaGrange et al., 2020), especially where more detailed facies models are developed (e.g. Kunzmann et al., 2019).

5.2. Authigenic vs hydrothermal sources of TEs in pyrite from the Teena subbasin

Depositional redox conditions and carbon export provided the main control on the sedimentary flux of Mo, Co and Ni (Fig. 10), which were then sequestered in varying proportions by pyrite as the long term sink (Fig. 13). The degree of trace metal pyritization (DTMP) for Ni and Co are reasonably consistent between the 6 samples from the Lower and Middle HYC units and similar to previous studies on anoxic sediments (Huerta-Diaz and Morse, 1992). The results also confirm that the LAICPMS data generated by the ablation of py1a aggregates are reasonably accurate and provide validation of the data processing method. There is a marked difference in the DTMP of Mo in samples from the Lower HYC unit (~20%) compared to the

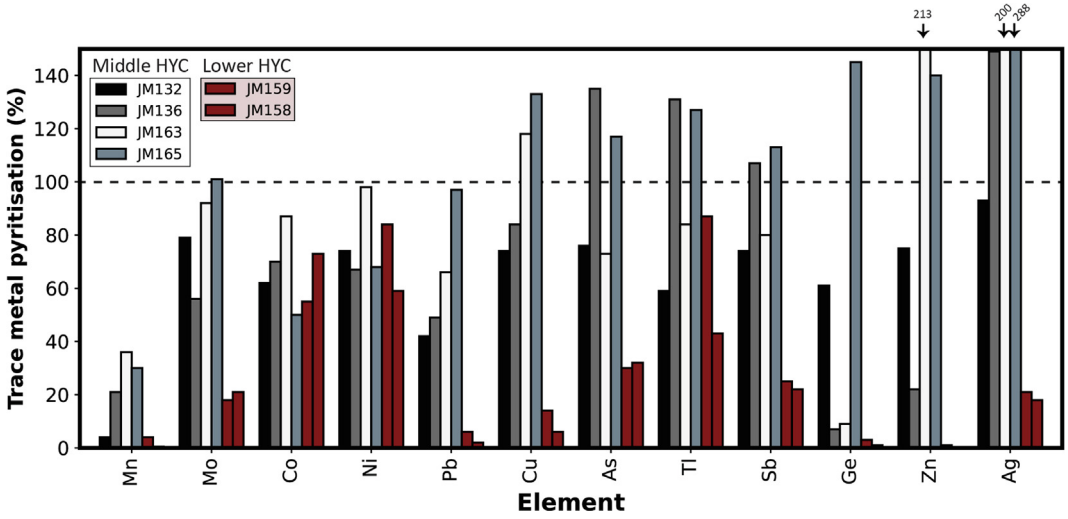

Fig. 13. The degree of trace metal pyritization (DTMP) calculated for 6 samples from the Middle HYC unit (n = 4) and Lower HYC unit (n = 2). The DTMP represents the fraction of the whole rock trace metal budget that is present in pyrite (Huerta-Diaz and Morse, 1992).

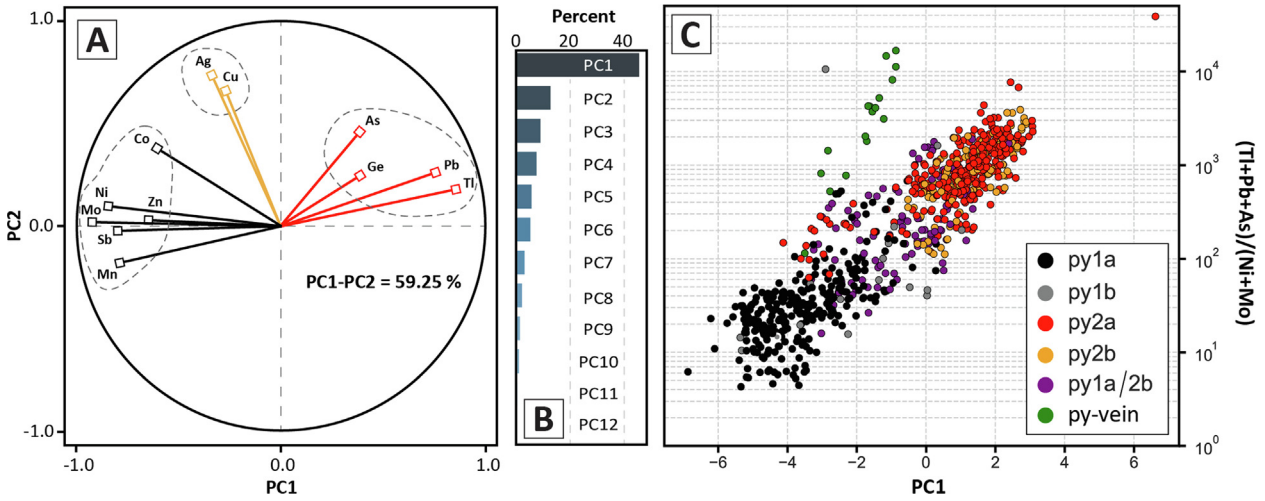

Fig. 14. (A) A projection of the scaled coordinates for PC1 and PC2 of each of the elements. (B) A vertical bar chart of all the principal components and the cumulative variance that they describe in the dataset. (C) A bivariate plot of all analyses showing PC1 vs. (Tl + Pb + As)/(Ni + Mo). The different colours correspond with the paragenetic stages of pyrite (see legend).

Middle HYC unit (>50%). The low DTMP values for Mo in the Lower HYC unit (~20%) indicate that pyrite is only a minor sink relative to carbonaceous material in the surrounding matrix (e.g. Chappaz et al., 2014). In contrast, the higher DTMP values for Mo in samples from the Middle HYC unit were selected from the euxinic interval overlying the B1 MFS, which may indicate an Fe-sulfide pathway of Mo sequestration under conditions of greater reduced sulfur availability (e.g. Vorlicek et al., 2018).

The hydrothermal pyrite (py2) preserves a different suite of elements to the diagenetic pyrite (Fig. 14). One of the main TEs that is enriched in py2 is As, which can also play an important role in controlling the incorporation of other TEs into pyrite (Deditius et al., 2008). Arsenic has three oxidation states that commonly substitute into the pyrite structure (As^{1-}, As^{2+}, and As^{3+}); under reducing conditions As^{1-} substitutes for S^{2-}, but under more oxidizing conditions divalent and trivalent As will substitute As^{3+} for Fe^{2+} (Reich et al., 2005; Deditius et al., 2008; Qian et al., 2013). The heterovalent substitution of As^{3+} for Fe^{2+} can facilitate the uptake of larger cations (e.g. Pb) due to lattice distortion and charge imbalance (Deditius et al., 2008), consistent with the negative correlation between Fe and As + Pb in py2 (Fig. 12). Further evidence of oxidising conditions is provided by the colloform morphology of py2, which was likely caused by changes in pyrite supersaturation that was sensitive to small changes in pH and fO_2 along the H_2S-SO_4^{2-} boundary (Butler and Rickard, 2000).

Pyrite can also host Tl from a few ppm to wt.% concentrations (Zhou et al., 2005; George et al., 2018). Notably, the Tl composition of py2 is almost two orders of magnitude greater than the suggested SEDEX composition (Fig. 11C). Thallium is highly incompatible and character-

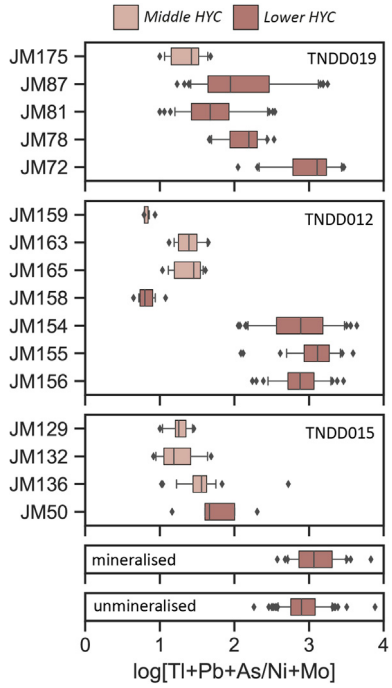

Fig. 15. A box and whisker plot showing (Tl + Pb + As)/(Ni + Mo) values for samples from the Teena subbasin, which have been ordered by increasing depth (top to bottom) and grouped according to the drill-holes (TNDD019, TNDD012, and TNDD019). The boxes define the interquartile range (25th to 75th percentile), solid circles and horizontal lines represent the average and median respectively, whiskers extend to the 5th and 95th percentile, and outliers are plotted as individual data points. The samples from TNDD015 preserve more uniform (Tl + Pb + As)/(Ni + Mo) values, whereas the samples in the other two drill-holes preserve much higher values towards (and within) the mineralized sequence. The mineralised and unmineralised samples at the bottom represent samples selected either side of the reaction interface from the sample in Fig. 9.

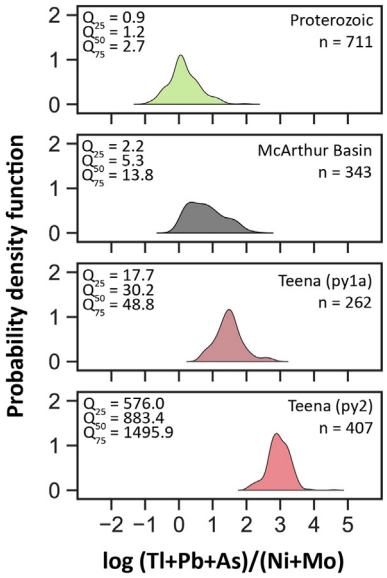

Fig. 16. Probability density functions for (Tl + Pb + As)/(Ni + Mo) values calculated for a compilation of pyrite data that has been grouped according to sample location. Data include analyses from Large et al., (2014), Mukherjee and Large (2017) and this study.

ized by both chalcophile and lithophile behaviour (McGoldrick et al., 1979; Baker et al., 2010). It is not known whether Tl is present within the pyrite crystal structure or as nano particles of Tl-bearing phases, although it has been suggested that Tl concentrations in pyrite are also highly dependent on the incorporation of As (Deditius and Reich, 2016). In the samples from Teena, however, there is no clear covariation between these 2 elements. Similarly, there is no covariation between Tl and Sb as would be expected from a mechanism involving coupled heterovalent substitution ($2Fe^{2+} = Tl^{+} + Sb^{3+}$; George et al., 2018). Alternatively, it may be that the pyrite incorporated nano-inclusions of monovalent Tl within structural defects (George et al., 2019), which, considering the smoothness of the ablation profiles, would have to be uniformly distributed. Kinetically-controlled TE incorporation requires pyrite growth rates that are great enough to exceed the equilibration and removal rate of TEs, which is supported by the porosity that is preserved in py2 (e.g. Fig. 6C, 7).

Thallium has two oxidation states (+1 and + 3), of which Tl^{+} is the most dominant and stable species in the sub-surface environment (Xiong, 2007). Monovalent Tl has a large ionic radius (1.5 Å), similar to K^{+}, Rb^{+} and Cs^{+}, meaning it is assumed to substitute into biotite and K-feldspar (Rehkämper and Nielsen, 2004). In modern mid ocean ridge hydrothermal systems, Tl is effectively leached from oceanic crust during fluid rock interaction (Metz and Trefry, 2000). A thick sequence of mafic volcanics in the stratigraphy underlying the BCF have been suggested as a source of base metals for the CD-type deposits in the southern McArthur Basin (Cooke et al., 1998), and so Tl may have a common source. Other potential sources of Tl in marine sedimentary rocks include Mn oxides and/or clay minerals (Nielsen et al., 2017; Martin et al., 2018). Previous studies have mapped Mn enrichment in the W-Fold Shale member underlying the HYC deposit, although this has been linked with hydrothermal input rather than authigenic Mn oxides (Large et al., 1998). Thallium could also be sourced via desorption from illite, which has a high exchange capacity at pH 7 (Martin et al., 2018). Determining which of the different stratigraphic components was the main source of Tl in the Teena subbasin could be tested through the analysis of Tl isotopes, considering the different isotopic fractionations involved with each source (Nielsen et al., 2017).

5.3. TE (TE) zonation around subseafloor hydrothermal systems

Recent studies on CD-type deposits in the southern McArthur Basin have reinforced decades old arguments that favour genesis via subseafloor replacement rather than SEDEX processes (Williams, 1978; Hayward et al., 2021; Spinks et al., 2021). High grade sulfide mineralization in

the Lower HYC unit formed when hydrothermal fluids were focused up and away from the Jabiru Fault at the time the overlying Middle HYC unit was deposited (Hayward et al., 2021). The decrease in (Tl + As + Pb)/(Mo + Ni) values in samples from TNDD012 and TNDD019 provides evidence of vertical TE zonation over a relatively short range (10^2-10^3 m), whereas pyrite from TNDD015 has relatively uniform (Tl + As + Pb)/(Mo + Ni) values (Fig. 15). The samples from TNDD012 and TNDD019 that preserve (Tl + As + Pb)/(Mo + Ni) values that are intermediate between the diagenetic and hydrothermal end members represent mixed ablations (py1a/2b). The mixed ablations are from samples located in the hangingwall sequence to the main sulfide lenses in the Lower HYC unit and are associated with microscopic hydrothermal overgrowths on the diagenetic pyrite (e.g. Fig. 6D and G).

Samples from the Middle HYC unit preserve significant variability in the DTMP values for elements associated with the hydrothermal end member (Pb, As, Tl, Sb, Ge, Zn, and Ag; Fig. 13). The variable DTMP values indicate that the LAICPMS analyses are not representative of the whole rock py1a composition, but rather the presence of other sulfide phases (e.g. sphalerite, galena, py2). In the SEDEX model, the formation of these sulfide phases in the Middle HYC unit would either be linked with distal hydrothermal activity in adjacent subbasins (e.g. HYC; Fig. 1) or a late stage of fluid exhalation from the Jabiru Fault. A more parsimonious explanation, however, is that hydrothermal fluids that were primarily focused in the Lower HYC unit also infiltrated the hangingwall sediments of the Middle HYC unit that were undergoing early diagenesis, resulting in discrete sulfide mineralization associated with pre-existing diagenetic pyrite.

More broadly, pyrite from the McArthur Basin contains (Tl + As + Pb)/(Mo + Ni) values that are intermediate between a compilation of Proterozoic pyrite and py1a from the Teena subbasin (Fig. 16). The range of (Tl + As + Pb)/(Mo + Ni) values is controlled primarily by the hydrothermal elements, as there is greater consistency in the Mo and Ni concentrations between the subgroups of data (Fig. 11). Many of the McArthur Basin samples were collected from subbasins characterized by varying degrees of hydrothermal anomalism (Fig. 1). For example, the Teena deposit is located in an adjacent subbasin to the McArthur River (HYC) deposit (Fig. 1), where a similar subseafloor replacement model has also been described (Spinks et al., 2021). The BCF in the Myrtle subbasin also contains CD-type sulfide mineralization (Mukherjee and Large, 2017). The interpretation of vertical TE zonation in the Teena subbasin (Fig. 15) provides important context for evaluating the trend towards high (Tl + As + Pb)/(Mo + Ni) values in the McArthur Basin (Fig. 16). It is entirely possible that hydrothermal TE anomalism in the BCF derives from vertical zonation contained by individual subbasins rather than lateral dispersal from exhalative systems in adjacent subbasins.

5.4. Implications

The nucleation of hydrothermal sulfide mineralization on pre-existing fine-grained pyrite is a common feature of modern and ancient subseafloor hydrothermal systems (Piercey, 2015; Nozaki et al., 2021). In the Teena subbasin, the overgrowth of hydrothermal sulfides on diagenetic pyrite is associated with TE anomalism that extends 100 s meters above the sulfide mineralization in the Lower HYC unit. In modern sediment hosted hydrothermal systems, the infiltration of hot fluids through organic rich sediments results in thermal degradation of organic matter, release of hydrocarbons and other organic compounds (e.g. Von Damm et al., 1985). The release of volatiles (CO_2, NH_4, CH_4) from organic matter degradation during hydrothermally accelerated diagenesis could have been particularly important for subsurface microbial ecosystems in the BCF (e.g. Nozaki et al., 2021).

In terms of the broader significance of the BCF in the context of mid-Proterozoic paleoenvironments, extrapolation of geochemical data generated from a single subbasin is clearly challenging. The careful integration of sequence stratigraphic data to augment geochemical data across the region will help to develop more comprehensive models of redox dynamics in the southern McArthur Basin. Nevertheless, there are similarities with other studies on mid-Proterozoic sedimentary units from intracontinental settings, where similar hydrographic factors controlled authigenic TE variability on a subbasin scale (e.g. Planavsky et al., 2018). Overall, the emerging paradigm is that bistability between ferruginous and euxinic redox end members was the result of weak redox buffers (i.e. low ferrous Fe and sulfide) and lower levels atmospheric oxygen (van de Velde et al., 2020b). Redox buffers in intracontinental settings (e.g. McArthur Basin) would have been particularly sensitive to hydrographic factors, resulting in regional heterogeneities and short term redox variability.

6. CONCLUSIONS

The intracontinental McArthur Basin contains exceptionally well-preserved mid-Proterozoic stratigraphy and is a classic locality for studies on giant Zn deposits and Proterozoic paleoenvironments. In the Teena subbasin, pyrite provides an archive of trace elements (TEs) that are associated with both biogenic and authigenic (e.g. Mo, Ni, Co) and hydrothermal (e.g. Tl, Pb, As) sources in the Teena subbasin. The formation of clastic dominant (CD-type) mineralization during burial diagenesis in the Teena subbasin has resulted in a complex paragenesis between diagenetic and hydrothermal pyrite. As a result, in situ analysis (LA-ICP-MS) was required to define compositional end members. A statistical analysis of pyrite chemistry in the Teena subbasin shows that increasing (Tl + As + Pb)/(Mo + Ni) values are associated with hydrothermal pyrite. Moreover, a gradual decrease in (Tl + As + Pb)/(Mo + Ni) values in the overlying hangingwall stratigraphy provides evidence of vertical zonation in Tl, Pb and As. In a comparison of literature data, diagenetic pyrite from the southern McArthur Basin preserves elevated (Tl + As + Pb)/(Mo + Ni) values relative to Proterozoic pyrite. The model developed for the Teena subbasin would ascribe the elevated (Tl + As + Pb)/(Mo + Ni) values to the dispersion of hydrothermal TEs into sediments undergoing diagenesis. In terms of whole rock data, covariation between total

organic carbon (TOC) and a different suite of TEs (Mo, Co, Ni, V) can be linked with water mass restriction during deposition of the hangingwall sedimentary units. The most organic rich facies (TOC > 2.5 wt.%) immediately overly the main maximum flooding surface in the Teena subbasin, where a correlation between high TOC/P values and sulfate limitation indicates the development of euxinic conditions. The subbasin scale (10^1 km^2) controls on TE variability highlights a key challenge when extrapolating from data collected in partially restricted intracontinental marine settings. Nevertheless, the evidence of stratigraphic redox bistability, between ferruginous (anoxic, non-sulfidic) and euxinic (sulfidic), is consistent with recent models for other mid-Proterozoic sedimentary units.

Declaration of Competing Interest

The authors declare that they have no known competing financial interests or personal relationships that could have appeared to influence the work reported in this paper.

ACKNOWLEDGEMENTS

We gratefully acknowledge funding for Joe Magnall's and Sarah Gleeson's research from a Helmholtz-Rekrutierungsinitive. Exploration work was funded by Teck, with contributions from Rox Resources Limited in the early stages. Teck also provided permission to publish. Franzi Wilke (GFZ) is gratefully acknowledged for help with EPMA analyses. Iain Dalrymple and Andrew Davies are thanked for early review comments. We also gratefully acknowledge Martin Reich (associate editor) and the detailed and constructive reviews from Dan Gregory, Marcus Kunzmann, Leslie Robbins, and Leonid Danyushevsky.

REFERENCES

Algeo T. J., Heckel P. H., Maynard J. B., Blakey R. and Rowe H. (2008) Modern and ancient epicratonic seas and the superestuarine circulation model of marine anoxia. In *Dynamics of Epeiric Seas: Sedimentological, Paleontological and Geochemical Perspectives* (eds. B. R. Pratt and C. Holmden). Geological Association of Canada Special Publications. pp. 7–38.

Algeo T. J. and Ingall E. (2007) Sedimentary Corg: P ratios, paleocean ventilation, and Phanerozoic atmospheric pO2. *Palaeogeogr. Palaeoclimatol. Palaeoecol.* **256**, 130–155.

Algeo T. J. and Lyons T. W. (2006) Mo-total organic carbon covariation in modern anoxic marine environments: Implications for analysis of paleoredox and paleohydrographic conditions. *Paleoceanography* **21**, 204–230.

Algeo T. J. and Maynard J. B. (2004) Trace-element behavior and redox facies in core shales of Upper Pennsylvanian Kansas-type cyclothems. *Chem. Geol.* **206**, 289–318.

Allen P. A., Eriksson P. G., Alkmim F. F., Betts P. G., Catuneanu O., Mazumder R., Meng Q. and Young G. M. (2015) Classification of basins, with special reference to Proterozoic examples. *Geol. Soc. Mem.* **43**, 5–28.

Baker R. G. A., Rehkämper M., Ihlenfeld C., Oates C. J. and Coggon R. (2010) Thallium isotope variations in an ore-bearing continental igneous setting: Collahuasi Formation, northern Chile. *Geochim. Cosmochim. Acta* **74**, 4405–4416.

Baruch E. T., Kennedy M. J., Löhr S. C. and Dewhurst D. N. (2015) Feldspar dissolution-enhanced porosity in Paleoproterozoic shale reservoir facies from the Barney Creek Formation (McArthur Basin, Australia). *Am. Assoc. Pet. Geol. Bull.* **99**, 1745–1770.

Berner R. A. (1984) Sedimentary pyrite formation: An update. *Geochim. Cosmochim. Acta* **48**, 605–615.

Betts P. G., Giles D. and Lister G. S. (2003) Tectonic environment of shale-hosted massive sulfide Pb-Zn-Ag deposits of proterozoic northeastern Australia. *Econ. Geol.* **98**, 557–576.

Betts P. G., Giles D., Mark G., Lister G. S., Goleby B. R. and Aillères L. (2006) Synthesis of the proterozoic evolution of the Mt. *Isa Inlier. Aust. J. Earth Sci.* **53**, 187–211.

Blaikie T. N. and Kunzmann M. (2020) Geophysical interpretation and tectonic synthesis of the Proterozoic southern McArthur Basin, northern Australia. *Precambrian Res.* **343** 105728.

Bradley D. C. (2008) Passive margins through earth history. *Earth-Science Rev.* **91**, 1–26.

Brocks J. J., Love G. D., Summons R. E., Knoll A. H., Logan G. A. and Bowden S. A. (2005) Biomarker evidence for green and purple sulphur bacteria in a stratified Palaeoproterozoic sea. *Nature* **437**, 866–870.

Butler I. B. and Rickard D. (2000) Framboidal pyrite formation via the oxidation of iron (II) monosulfide by hydrogen sulphide. *Geochim. Cosmochim. Acta* **64**, 2665–2672.

Chappaz A., Lyons T. W., Gregory D. D., Reinhard C. T., Gill B. C., Li C. and Large R. R. (2014) Does pyrite act as an important host for molybdenum in modern and ancient euxinic sediments? *Geochim. Cosmochim. Acta* **126**, 112–122.

Cooke D. R., Bull S. W., Donovan S. and Rogers J. R. (1998) K-metasomatism and base metal depletion in volcanic rocks from the McArthur basin, northern territory-implications for base metal mineralization. *Econ. Geol.* **93**, 1237–1263.

Cox G. M., Jarrett A., Edwards D., Crockford P. W., Halverson G. P., Collins A. S., Poirier A. and Li Z. X. (2016) Basin redox and primary productivity within the Mesoproterozoic Roper Seaway. *Chem. Geol.* **440**, 101–114.

Crick I. H., Boreham C. J., Cook A. C. and Powell T. G. (1988) Petroleum Geology and Geochemistry of Middle Proterozoic McArthur Basin, Northern Australia II: Assessment of Source Rock Potential. *Am. Assoc. Pet. Geol. Bull.* **72**, 1495–1514.

Von Damm K. L., Edmond J. M., Measures C. I. and Grant B. (1985) Chemistry of submarine hydrothermal solutions at Guaymas Basin. *Gulf of California. Geochim. Cosmochim. Acta* **49**, 2221–2237.

Danyushevsky L., Robinson P., Gilbert S., Norman M., Large R., McGoldrick P. and Shelley M. (2011) Routine quantitative multi-element analysis of sulphide minerals by laser ablation ICP-MS: Standard development and consideration of matrix effects. *Geochemistry Explor. Environ. Anal.* **11**, 51–60.

Deditius A. P. and Reich M. (2016) Constraints on the solid solubility of Hg, Tl, and Cd in arsenian pyrite. *Am. Mineral.* **101**, 1451–1459.

Deditius A. P., Utsunomiya S., Renock D., Ewing R. C., Ramana C. V., Becker U. and Kesler S. E. (2008) A proposed new type of arsenian pyrite: Composition, nanostructure and geological significance. *Geochim. Cosmochim. Acta* **72**, 2919–2933.

French K. L., Birdwell J. E., Vanden B. M. and D. (2020) Biomarker similarities between the saline lacustrine Eocene Green River and the Paleoproterozoic Barney Creek Formations. *Geochim. Cosmochim. Acta* **274**, 228–245.

Gadd M. G., Layton-Matthews D., Peter J. M. and Paradis S. J. (2016) The world-class Howard's Pass SEDEX Zn-Pb district, Selwyn Basin, Yukon. Part I: TE compositions of pyrite record input of hydrothermal, diagenetic, and metamorphic fluids to mineralization. *Miner. Depos.* **51**, 319–342.

Genna D. and Gaboury D. (2015) Deciphering the hydrothermal evolution of a VMS System by LA-ICP-MS using TEs in pyrite:

An example from the Bracemac-McLeod deposits, Abitibi, Canada, and implications for exploration. *Econ. Geol.* **110**, 2087–2108.

George L. L., Biagioni C., D'Orazio M. and Cook N. J. (2018) Textural and TE evolution of pyrite during greenschist facies metamorphic recrystallization in the southern Apuan Alps (Tuscany, Italy): Influence on the formation of Tl-rich sulfosalt melt. *Ore Geol. Rev.* **102**, 59–105.

George L. L., Biagioni C., Lepore G. O., Lacalamita M., Agrosì G., Capitani G. C., Bonaccorsi E. and d'Acapito F. (2019) The speciation of thallium in (Tl, Sb, As)-rich pyrite. *Ore Geol. Rev.* **107**, 364–380.

Giles D., Betts P. and Lister G. (2002) Far-field continental backarc setting for the 1.80-1.67 Ga basins of northeastern Australia. *Geology* **30**, 823–826.

Grant H. L. J., Hannington M. D., Petersen S., Frische M. and Fuchs S. H. (2018) Constraints on the behavior of TEs in the actively-forming TAG deposit, Mid-Atlantic Ridge, based on LA-ICP-MS analyses of pyrite. *Chem. Geol.* **498**, 45–71.

Gregory D. D., Cracknell M. J., Large R. R., McGoldrick P., Kuhn S., Maslennikov V. V., Baker M. J., Fox N., Belousov I., Figueroa M. C., Steadman J. A., Fabris A. J. and Lyons T. W. (2019) Distinguishing ore deposit type and barren sedimentary pyrite using laser ablation-inductively coupled plasma-mass spectrometry TE data and statistical analysis of large data sets. *Econ. Geol.* **114**, 771–786.

Gregory D. D., Lyons T. W., Large R. R., Jiang G., Stepanov A. S., Diamond C. W., Figueroa M. C. and Olin P. (2017) Whole rock and discrete pyrite geochemistry as complementary tracers of ancient ocean chemistry: An example from the Neoproterozoic Doushantuo Formation. *China. Geochim. Cosmochim. Acta* **216**, 201–220.

Guilbaud R., Poulton S. W., Thompson J., Husband K. F., Zhu M., Zhou Y., Shields G. A. and Lenton T. M. (2020) Phosphorus-limited conditions in the early Neoproterozoic ocean maintained low levels of atmospheric oxygen. *Nat. Geosci.* **13**, 296–301.

Hayward N., Magnall J. M., Taylor M., King R., McMillan N. and Gleeson S. A. (2021) The Teena Zn-Pb deposit (McArthur Basin, Australia). Part I: syndiagenetic base metal sulfide mineralization related to dynamic subbasin evolution. *Econ. Geol.* **116**, 1743–1768.

Huerta-Diaz M. A. and Morse J. W. (1992) Pyritization of trace metals in anoxic marine sediments. *Geochim. Cosmochim. Acta* **56**, 2681–2702.

Ingall E. D., Bustin R. M. and Van Cappellen P. (1993) Influence of water column anoxia on the burial and preservation of carbon and phosphorus in marine shales. *Geochim. Cosmochim. Acta* **57**, 303–316.

Ingham E. S., Cook N. J., Cliff J., Ciobanu C. L. and Huddleston A. (2014) A combined chemical, isotopic and microstructural study of pyrite from roll-front uranium deposits, lake eyre basin. *South Australia. Geochim. Cosmochim. Acta* **125**, 440–465.

Jackson M. J., Muir M. D. and Plumb K. A. (1987) Geology of the southern McArthur Basin, Northern Territory. eds. M. J. Jackson, M. D. Muir, and K. A. Plumb, Bureau of Mineral Resources, Canberra Bulletin. 220.

Johnston D. T., Farquhar J., Summons R. E., Shen Y., Kaufman A. J., Masterson A. L. and Canfield D. E. (2008) Sulfur isotope biogeochemistry of the Proterozoic McArthur Basin. *Geochim. Cosmochim. Acta* **72**, 4278–4290.

Johnston D. T., Poulton S. W., Dehler C., Porter S., Husson J., Canfield D. E. and Knoll A. H. (2010) An emerging picture of Neoproterozoic ocean chemistry: Insights from the Chuar Group, Grand Canyon, USA. *Earth Planet. Sci. Lett.* **290**, 64–73.

Keith M., Häckel F., Haase K. M., Schwarz-Schampera U. and Klemd R. (2016) TE systematics of pyrite from submarine hydrothermal vents. *Ore Geol. Rev.* **72**, 728–745.

Kunzmann M., Schmid S., Blaikie T. N. and Halverson G. P. (2019) Facies analysis, sequence stratigraphy, and carbon isotope chemostratigraphy of a classic Zn-Pb host succession: The Proterozoic middle McArthur Group, McArthur Basin. *Australia. Ore Geol. Rev.* **106**, 150–175.

LaGrange M. T., Konhauser K. O., Catuneanu O., Harris B. S., Playter T. L. and Gingras M. K. (2020) Sequence stratigraphy in organic-rich marine mudstone successions using chemostratigraphic datasets. *Earth-Science Rev.* **203** 103137.

Large R. R., Bull S. W., Cooke D. R. and Mcgoldrick P. J. (1998) A genetic model for the HYC deposit, Australia: Based on regional sedimentology, geochemistry, and sulfide-sediment relationships. *Econ. Geol.* **93**, 1345–1368.

Large R. R., Bull S. W., McGoldrick P. J., Walters S., Derrick G. M. and Carr G. R. (2005) Strata-Bound and Stratiform Zn-Pb-Ag Deposits in Proterozoic Sedimentary Basins, Northern Australia. *Econ. Geol.* **100**, 931–963.

Large R. R., Halpin J. A., Danyushevsky L. V., Maslennikov V. V., Bull S. W., Long J. A., Gregory D. D., Lounejeva E., Lyons T. W., Sack P. J., McGoldrick P. J. and Calver C. R. (2014) TE content of sedimentary pyrite as a new proxy for deep-time ocean-atmosphere evolution. *Earth Planet. Sci. Lett.* **389**, 209–220.

Li C., Planavsky N. J., Love G. D., Reinhard C. T., Hardisty D., Feng L., Bates S. M., Huang J., Zhang Q., Chu X. and Lyons T. W. (2015) Marine redox conditions in the middle Proterozoic ocean and isotopic constraints on authigenic carbonate formation: Insights from the Chuanlinggou Formation, Yanshan Basin, North China. *Geochim. Cosmochim. Acta* **150**, 90–105.

Liu J. and Algeo T. J. (2020) Beyond redox: Control of trace-metal enrichment in anoxic marine facies by watermass chemistry and sedimentation rate. *Geochim. Cosmochim. Acta* **287**, 296–317.

Longerich H. P., Jackson S. E. and Günther D. (1996) Inter-laboratory note. Laser ablation inductively coupled plasma mass spectrometric transient signal data acquisition and analyte concentration calculation. *J. Anal. At. Spectrom.* **11**, 899–904.

Magnall J. M., Gleeson S. A., Hayward N. and Rocholl A. (2020) Massive sulfide Zn deposits in the Proterozoic did not require euxinia. *Geochemical Perspect. Lett.* **13**, 19–24.

Magnall J. M., Hayward N., Gleeson S. A., Schleicher A., Dalrymple I., King R. and Mahlstadt N. (2021a) The Teena Zn-Pb deposit (McArthur Basin, Australia). Part II: carbonate replacement sulfide mineralization during burial diagenesis - implications for mineral exploration. *Econ. Geol.* **116**, 1769–1801.

Magnall J. M., Gleeson S. A., Hayward N. and Dalrymple I. (2021b) *Major, minor, and trace element lithogeochemistry of the Barney Creek Formation*. Carpentaria Province, northern Australia, GFZ Data Services, https://doi.org/10.5880/GFZ.3.1.2021.001

Magnall J. M., Oelze M. and Gleeson S. A. (2021c) Laser ablation inductively coupled mass spectrometry of pyrite from the Proterozoic Barney Creek Formation in the Teena subbasin (McArthur Basin, Australia). GFZ Data Services. https://doi.org/10.5880/GFZ.3.1.2021.002

Martin L. A., Wissocq A., Benedetti M. F. and Latrille C. (2018) Thallium (Tl) sorption onto illite and smectite: Implications for Tl mobility in the environment. *Geochim. Cosmochim. Acta* **230**, 1–16.

März C., Poulton S. W., Beckmann B., Küster K., Wagner T. and Kasten S. (2008) Redox sensitivity of P cycling during marine black shale formation: Dynamics of sulfidic and anoxic, non-

sulfidic bottom waters. *Geochim. Cosmochim. Acta* **72**, 3703–3717.

Maslennikov V. V., Maslennikova S. P., Large R. R. and Danyushevsky L. V. (2009) Study of TE zonation in vent chimneys from the silurian yaman-kasy volcanic-hosted massive sulfide deposit (Southern Urals, Russia) using laser ablation-inductively coupled plasma Mass Spectrometry (LA-ICPMS). *Econ. Geol.* **104**, 1111–1141.

McGoldrick P. J., Keays R. R. and Scott B. B. (1979) Thallium: a sensitive indicator of rock/seawater interaction and of sulfur saturation of silicate melts. *Geochim. Cosmochim. Acta* **43**, 1303–1311.

McGoldrick P., Winefield P., Bull S., Selley D. and Scott R. (2010) Sequences, Synsedimentary Structures, and Sub-Basins: the Where and When of SEDEX Zinc Systems in the Southern McArthur Basin. *Australia. Econ. Geol. Spec. Publ.* **15**, 367–389.

Metz S. and Trefry J. H. (2000) Chemical and mineralogical influences on concentrations of trace metals in hydrothermal fluids. *Geochim. Cosmochim. Acta* **64**, 2267–2279.

Mukherjee I. and Large R. (2017) Application of pyrite TE chemistry to exploration for SEDEX style Zn-Pb deposits: McArthur Basin, Northern Territory. *Australia. Ore Geol. Rev.* **81**, 1249–1270.

Nielsen S. G., Rehkämper M. and Prytulak J. (2017) Investigation and application of thallium isotope fractionation. *Rev. Mineral. Geochemistry* **82**, 759–798.

Nozaki T., Nagase T., Ushikubo T., Shimizu K., Ishibashi J. Ichiro (2021) Microbial Sulfate Reduction Plays an Important Role at the Initial Stage of SubSeafloor Sulfide Mineralization. *Geology* **49**, 222–227.

Page R. W., Jackson M. J. and Krassay A. A. (2000) Constraining sequence stratigraphy in north Australian basins: SHRIMP U-Pb zircon geochronology between Mt Isa and McArthur river. *Aust. J. Earth Sci.* **47**, 431–459.

Page R. W. and Sweet I. P. (1998) Geochronology of basin phases in the western Mt Isa Inlier, and correlation with the McArthur Basin. *Aust. J. Earth Sci.* **45**, 219–232.

Paton C., Hellstrom J., Paul B., Woodhead J. and Hergt J. (2011) Iolite: Freeware for the visualisation and processing of mass spectrometric data. *J. Anal. At. Spectrom.* **26**, 2508.

Piercey S. J. (2015) A semipermeable interface model for the genesis of subseafloor replacement-type volcanogenic massive sulfide (VMS) deposits. *Econ. Geol.* **110**, 488–489.

Planavsky N. J., McGoldrick P., Scott C. T., Li C., Reinhard C. T., Kelly A. E., Chu X., Bekker A., Love G. D. and Lyons T. W. (2011) Widespread iron-rich conditions in the mid-Proterozoic ocean. *Nature* **477**, 448–451.

Planavsky N. J., Slack J. F., Cannon W. F., O'Connell B., Isson T. T., Asael D., Jackson J. C., Hardisty D. S., Lyons T. W. and Bekker A. (2018) Evidence for episodic oxygenation in a weakly redox-buffered deep mid-Proterozoic ocean. *Chem. Geol.* **483**, 581–594.

Poulton S. W. and Canfeld D. E. (2011) Ferruginous conditions: A dominant feature of the ocean through Earth's history. *Elements* **7**, 107–112.

Qian G., Brugger J., Testemale D., Skinner W. and Pring A. (2013) Formation of As(II)-pyrite during experimental replacement of magnetite under hydrothermal conditions. *Geochim. Cosmochim. Acta* **100**, 1–10.

Rawlings D. J. (1999) Stratigraphic resolution of a multiphase intracratonic basin system: The McArthur Basin, northern Australia. *Aust. J. Earth Sci.* **46**, 703–723.

Redfield A. C. (1958) The biological control of chemical factors in the environment. *Am. Sci.* **46**, 205–221.

Rehkämper M. and Nielsen S. G. (2004) The mass balance of dissolved thallium in the oceans. *Mar. Chem.* **85**, 125–139.

Reich M., Deditius A., Chryssoulis S., Li J. W., Ma C. Q., Parada M. A., Barra F. and Mittermayr F. (2013) Pyrite as a record of hydrothermal fluid evolution in a porphyry copper system: A SIMS/EMPA TE study. *Geochim. Cosmochim. Acta* **104**, 42–62.

Reich M., Kesler S. E., Utsunomiya S., Palenik C. S., Chryssoulis S. L. and Ewing R. C. (2005) Solubility of gold in arsenian pyrite. *Geochim. Cosmochim. Acta* **69**, 2781–2796.

Reimann C., Filzmoser P., Garrett R. G. and Dutter R. (2008) Improving Data Behaviour for Statistical Analysis: Ranking and Transformations. *Stat. Data Anal. Explain.*, 167–179.

Reinhard C. T., Planavsky N. J., Gill B. C., Ozaki K., Robbins L. J., Lyons T. W., Fischer W. W., Wang C., Cole D. B. and Konhauser K. O. (2017) Evolution of the global phosphorus cycle. *Nature* **541**, 386–389.

Reinhard C. T., Planavsky N. J., Robbins L. J., Partin C. A., Gill B. C., Lalonde S. V., Bekker A., Konhauser K. O. and Lyons T. W. (2013) Proterozoic ocean redox and biogeochemical stasis. *Proc. Natl. Acad. Sci. U. S. A.* **110**, 5357–5362.

Rickard D. and Luther G. W. (2007) Chemistry of iron sulfides. *Chem. Rev.* **107**, 514–562.

Sageman B. B. and Lyons T. W. (2003) Geochemistry of Fine-grained Sediments and Sedimentary Rocks. In *Treatise on Geochemistry* (eds. H. D. Holland and K. K. Turekian). Elsevier. pp. 115–158.

Scholz F. (2018) Identifying oxygen minimum zone-type biogeochemical cycling in Earth history using inorganic geochemical proxies. *Earth-Science Rev.* **184**, 29–45.

Scholz F., McManus J. and Sommer S. (2013) The manganese and iron shuttle in a modern euxinic basin and implications for molybdenum cycling at euxinic ocean margins. *Chem. Geol.* **355**, 56–68.

Scott C., Lyons T. W., Bekker A., Shen Y., Poulton S. W., Chu X. and Anbar A. D. (2008) Tracing the stepwise oxygenation of the Proterozoic ocean. *Nature* **452**, 456–459.

Slomp C. P., Thomson J. and De Lange G. J. (2004) Controls on phosphorus regeneration and burial during formation of eastern Mediterranean sapropels. *Mar. Geol.* **203**, 141–159.

Southgate P. N., Bradshaw B. E., Domagala J., Jackson M., Idnurm M., Krassay A. A., Page R. W., Sami T. T., Scott D. L., Lindsay J. F., McConachie B. M. and Tarlowski C. Z. (2000) Chronostratigraphic framework for Palaeoproterozoic rocks (1730–1575Ma) in northern Australia and their implications for base-metal mineralisation. *Aust. J. Earth Sci.* **47**, 461–483.

Spinks S. C., Pearce M. A., Liu W., Kunzmann M., Ryan C. G., Moorhead G. F., Kirkham R., Blaikie T., Sheldon H. A., Schaubs P. M. and Rickard W. D. A. (2021) Carbonate Replacement as the Principal Ore Formation Process in the Proterozoic McArthur River (HYC) Sediment-Hosted Zn-Pb Deposit. *Australia. Econ. Geol.*, 1–26.

Stepanov A. S., Danyushevsky L. V., Large R. R., Mukherjee I. and Zhukova I. A. (2020) Deconvolution of the composition of fine-grained pyrite in sedimentary matrix by regression of time resolved LA-ICP-MS data. *Am. Mineral.* **105**, 820–832.

Tribovillard N., Algeo T. J., Lyons T. and Riboulleau A. (2006) Trace metals as paleoredox and paleoproductivity proxies: An update. *Chem. Geol.* **232**, 12–32.

Tyrrell T. (1999) The relative influences of nitrogen and phosphorus on oceanic primary production. *Nature* **400**, 525–531.

Van Cappellen P. and Ingall E. D. (1994) Benthic phosphorus regeneration, net primary production and ocean anoxia. *Paleoceanography* **9**, 677–692.

van de Velde S. J., Hylén A., Kononets M., Marzocchi U., Leermakers M., Choumiline K., Hall P. O. J. and Meysman F. J. R. (2020a) Elevated sedimentary removal of Fe, Mn, and TEs following a transient oxygenation event in the Eastern Gotland

Basin, central Baltic Sea. *Geochim. Cosmochim. Acta* **271**, 16–32.

van de Velde S. J., Reinhard C. T., Ridgwell A. and Meysman F. J. R. (2020b) Bistability in the redox chemistry of sediments and oceans. *Proc. Natl. Acad. Sci. U. S. A.* **117**, 33043–33050.

Vorlicek T. P., Helz G. R., Chappaz A., Vue P., Vezina A. and Hunter W. (2018) Molybdenum Burial Mechanism in Sulfidic Sediments: Iron-Sulfide Pathway. *ACS Earth Sp. Chem.* **2**, 565–576.

Wei W. and Algeo T. J. (2020) Secular variation in the elemental composition of marine shales since 840 Ma: Tectonic and seawater influences. *Geochim. Cosmochim. Acta* **287**, 367–390.

Williams N. (1978) Studies of the base metal sulfide deposits at McArthur River, Northern Territory, Australia; I, The Cooley and Ridge deposits. *Econ. Geol.* **73**, 1005–1035.

Wohlgemuth-Ueberwasser C. C., Ballhaus C., Berndt J., Stotter née Paliulionyte V. and Meisel T. (2007) Synthesis of PGE sulfide standards for laser ablation inductively coupled plasma mass spectrometry (LA-ICP-MS). *Contrib. to Mineral. Petrol.* **154**, 607–617.

Xiong Y. (2007) Hydrothermal thallium mineralization up to 300 ° C: A thermodynamic approach. *Ore Geol. Rev.* **32**, 291–313.

Zhou T. F., Fan Y., Yuan F., Wu M. A., Hou M. J., Voicu G., Hu Q. H., Zhang Q. M. and Yue S. C. (2005) A preliminary geological and geochemical study of the Xiangquan thallium deposit, eastern China: The world's first thallium-only mine. *Mineral. Petrol.* **85**, 243–251.

Associate editor: Martin Reich